

Parallel Continuous-Time Relative Localization with Augmented Clamped Non-Uniform B-Splines

Jiadong Lu^{†1,2}, Zhehan Li^{†1,2}, Tao Han³, Miao Xu^{2,4}, Chao Xu^{1,2}, and Yanjun Cao^{1,2}

Abstract—Accurate relative localization is critical for multi-robot cooperation. In robot swarms, measurements from different robots arrive asynchronously and with clock time-offsets. Although Continuous-Time (CT) formulations have proved effective for handling asynchronous measurements in single-robot SLAM and calibration, extending CT methods to multi-robot settings faces great challenges to achieve high-accuracy, low-latency, and high-frequency performance. Especially, existing CT methods suffer from the inherent query-time delay of unclamped B-splines and high computational cost. This paper proposes CT-RIO, a novel Continuous-Time Relative-Inertial Odometry framework. We employ Clamped Non-Uniform B-splines (C-NUBS) to represent robot states for the first time, eliminating the query-time delay. We further augment C-NUBS with closed-form extension and shrinkage operations that preserve the spline shape, making it suitable for online estimation and enabling flexible knot management. This flexibility leads to the concept of *knot-keyknot* strategy, which supports spline extension at high-frequency while retaining sparse keyknots for adaptive relative-motion modeling. We then formulate a sliding-window relative localization problem that operates purely on relative kinematics and inter-robot constraints. To meet the demanding computation required at swarm scale, we decompose the tightly-coupled optimization into robot-wise sub-problems and solve them in parallel using incremental asynchronous block coordinate descent. Extensive experiments show that CT-RIO converges from time-offsets as large as 263 ms to sub-millisecond within 3 s, and achieves RMSEs of 0.046 m and 1.8°. It consistently outperforms state-of-the-art methods, with improvements of up to 60% under high-speed motion.

Index Terms—Multi-robot systems, sensor fusion, localization, continuous-time trajectory.

I. INTRODUCTION

RECENTLY, multi-robot systems have been widely employed in diverse domains, including search and rescue [1]–[3] and environmental exploration [4], [5]. A fundamental capability enabling such tasks is relative localization within the swarm, which can be broadly categorized into indirect and direct approaches based on reliance on global information. Indirect methods typically use global information to compute relative poses. As shown in Fig. 1(a), a classic method is to estimate each robot’s global pose, and then compute relative poses by aligning their respective reference frames [6]–[13].

[†] Equal contribution.

¹ State Key Laboratory of Industrial Control Technology, Institute of Cyber-Systems and Control, Zhejiang University, Hangzhou, 310027, China.

² Huzhou Institute of Zhejiang University, Huzhou, 313000, China.

³ The School of Automation and Intelligent Sensing, Shanghai Jiao Tong University, Shanghai, 200240, China.

⁴ Department of Automatic Control, Faculty of Engineering, Lund University, Lund, 22100, Sweden.

This work was supported by National Nature Science Foundation of China under Grant 62103368. The corresponding author is Yanjun Cao.

E-mails: {jdlu, zhehanli, yanjunhi}@zju.edu.cn

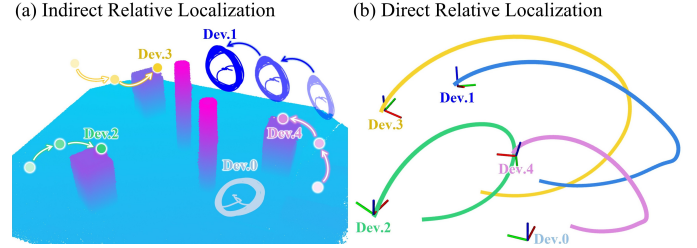


Fig. 1. Comparison between typical indirect and direct relative localization. (a) Trajectories are estimated in separate reference frames and aligned to a global consensus. (b) Relative trajectories are estimated in a robocentric frame.

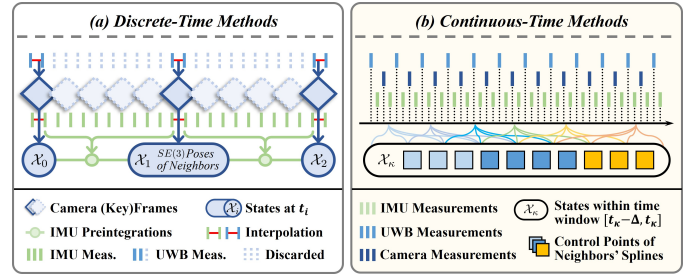


Fig. 2. Comparison between discrete-time and continuous-time relative localization methods. (a) Discrete-time methods estimate states $\{X_0, X_1, \dots\}$ only at camera keyframes. Asynchronous measurements (e.g., UWB) are temporally interpolated to keyframe timestamps, IMU data are summarized via pre-integration, and intermediate frames and measurements are discarded. (b) Continuous-time methods parameterize the state X_c with B-splines, allowing all measurements to directly constrain the trajectory at their native timestamps.

In contrast, direct relative localization estimates relative states solely from inter-robot observations, without requiring any global information [14]–[26]. Such methods often adopt a robocentric formulation as illustrated in Fig. 1(b).

Direct relative localization can be achieved using sensors such as AprilTag [14], LED markers [15]–[17], or UWB arrays [18]–[20]. Recent works [22]–[26] demonstrate that incorporating IMU significantly improves both accuracy and robustness. An optimization-based framework, CREPES-X [25], tightly couples distance, bearing, and inertial measurements and reports state-of-the-art accuracy in direct relative localization. However, its discrete-time nature limits its performance.

In multi-robot systems, two challenges arise in discrete-time relative localization: (i) *Asynchronous measurements*: Sensors on different robots often operate at varying rates and are unaligned, making it impossible to find the measurements at a specific time for data fusion; thus, extensive interpolation and data discarding are required. As shown in Fig. 2(a), this would discard valuable inter-frame observations and distort the value and covariance of the measurements [25], degrading estimation accuracy. (ii) *Inter-robot time-offsets*: Different robots often

operate with unsynchronized system clocks. Some existing multi-robot systems rely solely on network synchronization, whose errors can reach the order of 10^2 ms [27], while others eliminate offsets using dedicated hardware such as UWB [22], [25]. To avoid additional hardware, several approaches estimate time-offsets by assuming constant velocity over short intervals and deriving time-offset-related residuals [26], [28]. However, this assumption is often violated in highly dynamic multi-robot settings.

Continuous-time representation: In contrast to discrete-time formulations, trajectories can be parameterized in continuous time using B-splines. This representation naturally supports high-rate, multi-rate, and asynchronous sensor measurements without requiring data interpolation or sample dropping (Fig. 2(b)). Moreover, the availability of analytic B-spline derivatives enables joint estimation of time-offsets directly from motion, without introducing additional motion assumptions. This property has been successfully exploited for sensor time synchronization for single-robot [29], [30]. Owing to these advantages, continuous-time B-spline trajectory representations have become increasingly popular in both calibration tasks [31]–[34] and SLAM [29], [35]–[42]. Recent advances further demonstrate that non-uniform knot placement can significantly improve both accuracy and computational efficiency [40]. In multi-robot systems, where motion characteristics and relative motion intensity may vary substantially across robots, Non-Uniform B-Splines (NUBS) are particularly well suited. They allow modeling capacity to be concentrated in dynamically rich segments of motion while avoiding redundant representation in less informative regions.

However, a fundamental challenge hinders the adoption of NUBS in multi-robot systems. Existing NUBS-based methods employ an unclamped formulation, which inevitably introduces query delay to the latest sensor timestamp, since the state cannot be evaluated beyond the latest fully supported knot interval, as shown in Fig. 3(a). To address this limitation, we adopt Clamped Non-Uniform B-Splines (C-NUBS) in continuous-time state estimation for the first time. By repeating boundary knots, C-NUBS clamp the evaluation range at the latest knot and thereby eliminate the intrinsic query delay of unclamped splines, as illustrated in Fig. 3(b).

While clamping resolves the latency issue, it introduces a new challenge for incremental state estimation. Specifically, adding/removing the last spline segment alters the former spline shape, breaking the consistency of previously optimized trajectory segments. We overcome this limitation by deriving analytic spline extension and shrinkage operators that preserve the spline shape exactly, allowing new spline segments to be appended or removed flexibly without affecting existing estimates. Building on this flexibility, we propose a *knot-keyknot* strategy, in which knots are added at high frequency while only sparse keyknots are retained within a sliding window to ensure computational efficiency, analogous to the frame-keyframe structure in discrete-time systems.

Nevertheless, continuous-time multi-robot optimization remains computationally heavy because residuals couple many control points across trajectories. We decompose the global problem into robot-wise subproblems, each solvable within

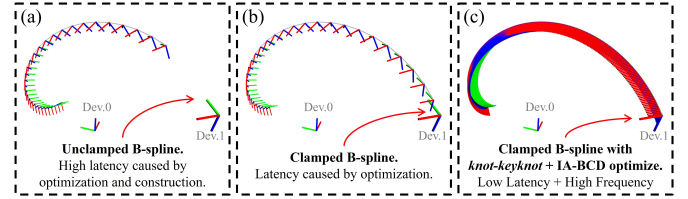


Fig. 3. Visualization of output frequency and latency using (a) unclamped B-spline, (b) clamped B-spline, and (c) clamped B-spline with knot-keyknot strategy and IA-BCD optimization.

TABLE I: MULTI-ROBOT RELATIVE LOCALIZATION ALGORITHMS

State Representation	No Interpolate	No Discard	Time-Offset Esti.
Discrete-Time	✗	✗	◇
Continuous-Time	✓	✓	✓
Continuous-Time Knot Freq.	Adaptive Knot	High Accuracy	High Efficiency
Uniform	✗	✗	✗
Non-Uniform	✓	✓	✓
Non-Uniform B-Spline Type	No Query-Delay	High Freq.	Instant Output
Unclamped	✗	✗	✗
Clamped	✓	✗	✗
+ <i>knot-keyknot</i>	✓	✓*	✗
+ IA-BCD	✓	✗	✓
+ IA-BCD + <i>knot-keyknot</i>	✓	✓	✓

◇ Some discrete-time methods [28] estimate time-offsets by assuming constant velocity between frames. * Limited by optimization time.

milliseconds, yielding a Block Coordinate Descent (BCD) formulation with one trajectory per block. A distinctive feature of our approach is the exploitation of the trajectory’s temporal structure: as new knots are incrementally appended, the corresponding subproblems are triggered for immediate re-optimization. Each subproblem is solved in a separate thread without waiting for other subproblems to complete their updates, eliminating the costly idle time and enabling high-frequency output for each robot with minimal latency, as illustrated in Fig. 3(c). Despite the lack of explicit variable synchronization, we derive that this Incremental Asynchronous BCD (IA-BCD) scheme converges to a stationary point of the full problem under appropriate step-size conditions.

The advantages of the above developments are summarized in Tab. I. Based on these, we present a Continuous-Time Relative-Inertial Odometry (CT-RIO) framework which is designed for high-accuracy, low-latency, and high-frequency estimation of relative poses and inter-robot time-offsets.

Our main contributions are summarized as follows:

- 1) We introduce C-NUBS into continuous-time state estimation, eliminating the intrinsic query delay of NUBS-based methods, and derive closed-form extension and shrinkage operators that preserve the curve shape. And we further proposed a *knot-keyknot* strategy to extend the spline at high frequency while retaining sparse keyknots, enabling high-rate outputs and improving efficiency.
- 2) We formulate the general continuous-time direct relative localization as a factor-graph optimization problem under robocentric relative kinematics, incorporating inter-robot constraints and motion constraints, thereby enabling the joint estimation of 6-DoF relative poses and inter-robot time offsets.
- 3) We propose **CT-RIO**, a C-NUBS-based framework

that adaptively allocates modeling capacity via motion-intensity-aware keyknot selection, and solves robot-wise sub-problems in parallel using IA-BCD, achieving real-time performance while retaining high accuracy.

- 4) We validate CT-RIO in extensive simulations and real-world experiments, demonstrating that it outperforms the state-of-the-art discrete-time method.

The remainder of this paper is organized as follows: Sec. II reviews the relevant literature. Sec. III introduces the preliminaries and augmentations of C-NUBS. Sec. IV formulates the continuous-time direct relative localization problem and decomposes it into robot-wise sub-problems. Building on these, Sec. V details the proposed C-NUBS-based relative localization system CT-RIO. Then, Sec. VI validates the system components in simulations, while Sec. VII demonstrates the effectiveness of CT-RIO in real-world experiments. Finally, Sec. VIII concludes this work and discusses future directions.

II. RELATED WORKS

A. Direct Relative State Estimation

Direct relative localization has attracted significant attention due to its self-sufficiency, stability, efficiency, and accuracy. Given space limitations, this review focuses on direct relative localization methods based on multi-sensor fusion.

Existing multi-sensor fusion approaches can be broadly categorized as loosely or tightly coupled. Both paradigms model relative kinematics in the robocentric frame and fuse them with inertial measurements. Loosely-coupled approaches typically partition a multi-robot system into multiple pairwise subsystems [21]–[24], which limits their ability to exploit swarm correlations. To better leverage group-level couplings, tightly-coupled relative state estimation has been widely studied. [43] fused the anonymous bearing with inertial data via a particle filter to recover the scale and relative poses. [26] proposed passive UWB ranging and an on-manifold EKF that tightly couples UWB distance measurements with IMU pre-integration to jointly estimate the relative state on $SE_2(3)$. [25] proposed a tightly-coupled least-squares optimization to fuse distance, bearing, and inertial measurements, and reports improved robustness in non-line-of-sight environments. However, filtering-based methods often struggle to enforce global consistency, while discrete-state optimization typically relies on interpolating asynchronous measurements and discarding high-rate observations, leading to information loss.

A further challenge in relative localization is the time-offsets caused by independent system clocks across robots. Without dedicated synchronization hardware, these offsets can reach the order of 10^2 ms [27], significantly degrading localization accuracy. Online time-offset estimation has been explored in single robot SLAM for cross-sensor calibration, typically exploiting short-horizon constant-velocity assumptions to construct time-offset-related residuals [44], [45]. These ideas have been extended to multi-robot relative localization. For example, [26] modeled the UWB clock offset as an explicit state within an on-manifold EKF. Meanwhile, in an indirect setting, [28] formulated time-offset-induced bearing projection errors and solved the resulting problem via SDP. However,

this assumption is often violated in multi-robot settings, where relative motions between robots can be highly dynamic.

These problems motivate continuous-time formulations that handle asynchronous measurements in a principled manner.

B. Continuous-Time State Estimation

Continuous-time representations include linear interpolation, wavelets, Gaussian processes, and splines. In this paper, we focus on B-spline-based representation. [46] systematically proposed the B-spline-based continuous-time SLAM problem and demonstrated its application in the self-calibration of the IMU-camera extrinsic parameters. Thereafter, B-spline-based continuous-time trajectory formulations have been widely used in sensor calibration [31]–[34] and SLAM-related applications [29], [35]–[42]. [30] conducted a comprehensive comparison between continuous-time and discrete-time methods, highlighting that the knot distribution has a significant impact on estimation performance and computational efficiency. [40] introduced a motion-adaptive scheme that outperforms uniform placement, which was later extended to a Gaussian Splatting SLAM system in [42]. A similar approach was explored in [47] for UWB anchor-based odometry. However, due to the recursive construction of B-splines, existing unclamped B-spline-based non-uniform methods inevitably suffer from a query-time delay, as discussed in Sec. III-B.

Beyond motion representation, a key advantage of B-spline-based trajectory formulation is its natural support for online time-offset estimation. Unlike discrete-time methods, which rely on short-term constant-velocity assumptions, continuous-time approaches exploit the analytically differentiable structure of the trajectory. This enables querying pose and velocity at arbitrary timestamps, allowing the time-offset to be directly embedded into the measurement model and simplifying the computation of associated Jacobians. Consequently, time-offsets can be jointly optimized with the trajectory without introducing additional motion assumptions [29], [34], [46]. Empirical studies [30] further report that continuous-time formulations yield significantly higher accuracy in time-offset estimation than discrete-time methods.

To the best of our knowledge, no prior work has investigated continuous-time direct relative localization. CT-RIO extends continuous-time state estimation to multi-robot settings to naturally retain high-frequency sensor information while supporting online inter-robot time-offset estimation. The closest prior work is [47], which studies UWB anchor-based odometry with fixed infrastructure, fundamentally differing from fully mobile multi-robot relative localization. Moreover, it adopts unclamped non-uniform B-splines similar to [40], which incur query-time latency. In contrast, CT-RIO builds upon C-NUBS to eliminate the delays and further address the spline shape variations introduced by C-NUBS during spline extension and shrinkage, as detailed in Sec. III.

C. Acceleration Methods in Swarm Robot State Estimation

Achieving scalable state estimation across a robot swarm is an indispensable objective and has been actively studied in both indirect and direct relative localization paradigms.

In indirect relative localization, [48] operated on factor graphs that rely on Gaussian elimination and require robots to exchange Gaussian marginals about shared variables. [49] employed ADMM for distributed SLAM. [50], [51] used Gaussian belief propagation to perform localization. Meanwhile, many recent advancements in multi-robot localization leverage advances in distributed pose-graph optimization (PGO). [52] proposed SDP relaxation together with Riemannian BCD, which enables verification of the correctness of the estimates, and is decentralized and asynchronous. More recently, [53] used distance measurements and showed that it is possible to obtain certifiably optimal solutions again via SDP relaxation.

In direct relative localization, recent studies have investigated both distributed and centralized frameworks for fusing UWB array and IMU data to enhance scalability. On the distributed side, [54] proposed a scheme where each robot estimates the relative poses of its neighbors in its own frame. By broadcasting these local estimates and employing SDP-based alignment, individual local topologies are merged into a consistent global configuration. On the centralized side, [55] formulated the relative state estimation problem as a generalized graph realization and solved the resulting multi-convex optimization using BCD for scalability.

While these approaches achieve scalability for discrete-time methods, they either rely on synchronized updates in optimization or cannot be directly extended to continuous-time formulations. [56] established the theoretical foundation of Asynchronous BCD (A-BCD), analyzing its convergence under both bounded and unbounded delays, thereby eliminating the system latency and speed limitations induced by synchronized updates. Motivated by this line of work, we adopt an Incremental A-BCD (IA-BCD) variant within CT-RIO to enable asynchronous, parallel solution of agent-wise subproblems in a tightly-coupled continuous-time estimator.

III. AUGMENTED C-NUBS FOR STATE ESTIMATION

This section details the continuous-time trajectory representation underpinning CT-RIO. We first introduce the preliminaries of NUBS, then discuss the properties of clamped construction. Based on these properties, we derive closed-form extension and shrinkage methods for C-NUBS to preserve the spline shape, augmenting it to support state estimation applications. Finally, we propose a *knot-keyknot* strategy for C-NUBS-based continuous-time state estimation.

A. Preliminary of Non-Uniform B-Splines

In CT-RIO, we employ cumulative NUBS for relative poses that separately parameterize the rotations $\mathbf{R}(t) \in SO(3)$ and translations $\mathbf{p}(t) \in \mathbb{R}^3$. The translation NUBS curve of order k (or degree $k-1$) with n control points is defined by a knot vector $\mathbf{T} = \{t_{[0]}, t_{[1]}, \dots, t_{[n+k]}\}$ and control points $\mathbf{x}_{\mathbf{p}} = \{\mathbf{p}_0, \mathbf{p}_1, \dots, \mathbf{p}_n\}$. See Appendix A-A for more details about the definition of B-splines. Due to the local support property of NUBS, whereby only k control points influence the curve value at any time t , the curve admits a compact matrix

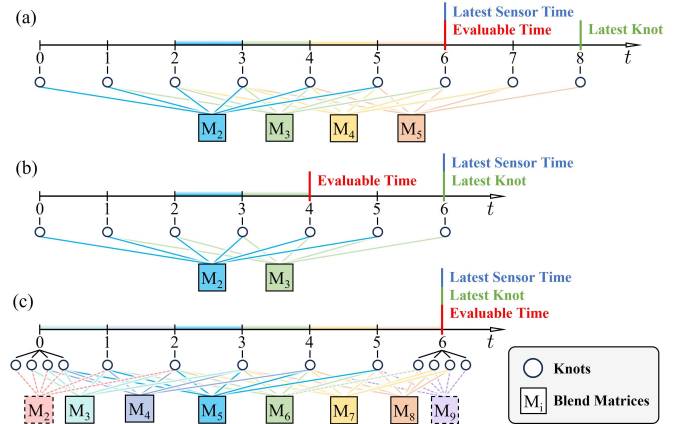


Fig. 4. Three different spline parameterizations ($k = 4$) with the earliest sensor time at 0s and the latest sensor time at 6s. The unclamped B-splines benefit from the *Extended Query Interval Property*, which provides one additional evaluable segment. (a) Uniform B-spline. (b) Unclamped non-uniform B-spline. (c) Clamped non-uniform B-spline.

representation [57]. The value of $\mathbf{p}(t)$ at time $t \in [t_{[i]}, t_{[i+1]})$ can be expressed as:

$$\underbrace{\mathbf{p}(t)}_{3 \times 1} = \underbrace{\left[\mathbf{p}_{i-k+1}, \mathbf{d}_{i-k+1}^{(1)}, \dots, \mathbf{d}_{i-k+1}^{(k-1)} \right]}_{3 \times k} \underbrace{\widetilde{\mathbf{M}}_i^{(k)}}_{k \times k} \underbrace{\mathbf{u}}_{k \times 1}, \quad (1)$$

$$\mathbf{u} = [1 \quad u \quad \dots \quad u^{k-1}], \quad u = (t - t_{[i]}) / (t_{[i+1]} - t_{[i]}),$$

with difference vectors $\mathbf{d}_i^{(j)} = \mathbf{p}_{i+j} - \mathbf{p}_{i+j-1}$. The cumulative blend matrix $\widetilde{\mathbf{M}}_i^{(k)}$ is only related to order k and $2(k-1)$ knots $\{t_{[i-k+2]}, \dots, t_{[i+k-1]}\}$, see Appendix A-B for more details.

Cumulative NUBS can be generalized to Lie groups and, in particular, to $SO(3)$ for smooth rotation generation [58]. Similar to (1), we can represent the cumulative rotation NUBS with control points $\mathbf{x}_{\mathbf{R}} = \{\mathbf{R}_0, \mathbf{R}_1, \dots, \mathbf{R}_n\}$ of order k over time $t \in [t_{[i]}, t_{[i+1]})$ as:

$$\mathbf{R}(t) = \mathbf{R}_{i-k+1} \cdot \prod_{j=1}^{k-1} \text{Exp} \left(\widetilde{\mathbf{M}}_i^{(k)} \mathbf{u} \cdot \mathbf{d}_{i-k+1}^{(j)} \right), \quad (2)$$

where $\mathbf{d}_i^{(j)} = \text{Log}(\mathbf{R}_{i+j-1}^{-1} \mathbf{R}_{i+j})$, and $\mathbf{R}_i \in SO(3)$ is the i -th rotation control point. $\text{Exp}(\cdot)$ and $\text{Log}(\cdot)$ are the exponential and logarithmic maps of $SO(3)$.

As can be seen from (1) and (2), the valid query range of an NUBS is smaller than the bounds of its knot vector. Specifically, only the intervals where the blend matrix can be constructed are valid, with each blend matrix corresponding to one spline segment. Thus, if $t_{[n+k]}$ is the most recent knot, the spline is only defined up to $t_{[n+1]}$, introducing an inherent delay of $(t_{[n+k]} - t_{[n+1]})$.

Extended Query Interval Property: For a B-spline of order k with knot vector $\mathbf{T} = \{t_{[0]}, t_{[1]}, \dots, t_{[n+k]}\}$, the actual valid query interval is $[t_{[k-2]}, t_{[n+2]})$, with a query delay of $(t_{[n+k]} - t_{[n+2]})$. See Appendix A-C for more details.

B. Clamped Non-Uniform B-Splines

C-NUBS are a classical variant of NUBS in which the first and last knots are repeated k times, forcing the curve

to interpolate its endpoints [59]:

$$\begin{aligned} \mathbf{T}_{\text{clamp}} : t_{[0]} = \dots = t_{[k-1]} \leq \dots \leq t_{[n+1]} = \dots = t_{[n+k]}, \\ \mathbf{T}_{\text{unclamp}} : t_{[0]} \leq t_{[1]} \leq \dots \leq t_{[n+k-1]} \leq t_{[n+k]}. \end{aligned} \quad (3)$$

This formulation provides the same approximation capability as the unclamped version while yielding improved boundary behavior and has been widely used in computer graphics [59] and path planning [60]. In real-time state estimation, clamping can eliminate the inherent evaluation delays at the curve endpoints, which is rarely discussed in prior works [40], [42], [47] but is crucial for online applications.

For uniform B-splines, subsequent knots and control points can be generated in advance. This eliminates the inherent delay and extends the valid range of the B-spline to the latest sensor time, enabling real-time optimization. As shown in Fig. 4(a), evaluating the spline at time $6s$ requires the knots and control points at time $7s$ and $8s$ to be available in advance.

However, for NUBS, since knot intervals are uncertain and typically determined by the latest sensor measurements [40], [42], it is impossible to generate knots and control points beyond the latest sensor time in advance. As a result, estimation must inevitably suffer from the inherent delay. As shown in Fig. 4(b), although exploiting the *Extended Query Interval Property*, the spline can only be evaluated up to time $4s$, resulting in a delay of $2s$.

For C-NUBS, the repeated final knot allows immediate evaluation up to the latest time, directly eliminating the inherent delay. This property enables adaptive insertion of non-uniform knots and control points in response to incoming sensor data, while still providing state estimates at the most recent knot time. As shown in Fig. 4(c), the latest sensor time, the latest knot time, and the evaluable time all coincide at $6s$.

Moreover, C-NUBS also ensures that the curve passes through the final control point, which is useful for initializing new segments. However, adding or deleting the last control point changes the shape of the last $(k-1)$ segments, which is undesirable for consistent state estimation.

C. Closed-Form Extension of C-NUBS

A significant issue of C-NUBS is that when new control points are added, the original part will change, causing a shift in the convergence result of the previous optimization. An iterative unclamping algorithm is proposed in [59], which has been successfully applied in [61]. [61] determines the extended knot based on chord length estimation, aiming to maintain low curvature in the newly added segment under varying distances to the target control point. In contrast, for state estimation, the goal is to accurately parameterize the state at a specified time, requiring explicit specification of both the target knot and control point. We achieve this by adjusting only the last $k-2$ control points, a process we term closed-form extension.

Proposition 1 (Closed-form extension of a C-NUBS). *Consider a C-NUBS curve of order k be defined by control points \mathbf{x}_p and a clamped knot vector \mathbf{T} :*

$$\begin{aligned} \mathbf{x}_p = \{\mathbf{p}_0, \mathbf{p}_1, \dots, \mathbf{p}_{n-k-1}, \mathbf{p}_{n-k}, \dots, \mathbf{p}_n\}, \\ \mathbf{T} : t_{[0]} = \dots = t_{[k-1]} \leq \dots \leq t_{[n+1]} = \dots = t_{[n+k]}. \end{aligned} \quad (4)$$

An extension of this C-NUBS to a new knot $t_{[n+k+1]}$ with a new control point $\tilde{\mathbf{p}}_{n+1}$ is obtained through the following transformation:

1) *Replace the last $k-1$ knots with $t_{[n+k+1]}$:*

$$\mathbf{T}' : t_{[0]} = \dots = t_{[k-1]} \leq \dots \leq t_{[n+2]} = \dots = t_{[n+k]}.$$

2) *Update the last $k-2$ control points $\tilde{\mathbf{p}}_{n-k+3}, \dots, \tilde{\mathbf{p}}_n$ by the unclamping algorithm to keep the original shape:*

$$\mathbf{x}_p' = \{\mathbf{p}_0, \mathbf{p}_1, \dots, \mathbf{p}_{n-k+2}, \tilde{\mathbf{p}}_{n-k+3}, \dots, \tilde{\mathbf{p}}_n\},$$

3) *Append the new control point $\tilde{\mathbf{p}}_{n+1}$ and the new knot $t_{[n+k+1]}$ at the end of the modified curve:*

$$\mathbf{x}_p'' = \{\mathbf{p}_0, \mathbf{p}_1, \dots, \mathbf{p}_{n-k+2}, \tilde{\mathbf{p}}_{n-k+3}, \dots, \tilde{\mathbf{p}}_n, \tilde{\mathbf{p}}_{n+1}\},$$

$$\mathbf{T}'' : t_{[0]} = \dots = t_{[k-1]} \leq \dots \leq t_{[n+2]} = \dots = t_{[n+k+1]},$$

The resulting C-NUBS $(\mathbf{x}_p'', \mathbf{T}'')$ is identical to the original curve on $[t_{[0]}, t_{[n+k]}]$ and is extended to $t_{[n+k+1]}$ with the control point $\tilde{\mathbf{p}}_{n+1}$. The full algorithm is summarized in Alg. 1.

Algorithm 1 Closed-Form Extension of C-NUBS

Input: A C-NUBS parameterize by $(\mathbf{x}_p, \mathbf{T})$. Target control point $\tilde{\mathbf{p}}_{n+1}$ and target knot $t_{[n+k+1]}$.

Output: Extended C-NUBS $(\mathbf{x}_p'', \mathbf{T}'')$.

1: Let $\mathbf{T}' =$

$$\{t_{[0]} = \dots = t_{[k-1]} \leq \dots \leq t_{[n+2]} = \dots = t_{[n+k]}\}.$$

2: Set initial value. Let: $\tilde{\mathbf{p}}_i^0 = \mathbf{p}_i, i = n-k+2, \dots, n$.

3: **for** $r = 1$ to $k-2$ **do**

4: **for** $i = n-k+2$ to $n-r$ **do**

5: $\tilde{\mathbf{p}}_i^r = \tilde{\mathbf{p}}_i^{r-1}$

6: **end for**

7: **for** $i = n-r+1$ to n **do**

8: $\alpha_{i,r} = (\mathbf{T}'_{n+1} - \mathbf{T}'_i) / (\mathbf{T}'_{i+r+1} - \mathbf{T}'_i)$.

9: $\tilde{\mathbf{p}}_i^r = (\tilde{\mathbf{p}}_i^{r-1} - (1 - \alpha_{i,r})\tilde{\mathbf{p}}_{i-1}^{r-1}) / \alpha_{i,r}$.

10: **end for**

11: **end for**

12: Let

$$\mathbf{x}'_{p_i} = \begin{cases} \mathbf{p}_i, & i = 0, 1, \dots, n-k+1 \\ \tilde{\mathbf{p}}_i^{k-2}, & i = n-k+2, \dots, n \end{cases}$$

13: Append $(\tilde{\mathbf{p}}_{n+1}, t_{[n+k+1]})$ to $(\mathbf{x}'_p, \mathbf{T}')$ and obtain $(\mathbf{x}_p'', \mathbf{T}'')$.

14: **return** $\mathbf{x}_p'', \mathbf{T}''$.

Proof. As shown in [59], the last $k-1$ knots of a C-NUBS can be reassigned arbitrarily if the last $k-2$ control points are iteratively updated to preserve the curve shape. Following this principle, the last $k-1$ knots are first replaced with the new knot $t_{[n+k+1]}$, temporarily converting the clamped spline into an unclamped one. The last $k-2$ control points are then updated using the unclamping procedure to maintain shape invariance. After this operation, the curve over the existing domain $[t_{[0]}, t_{[n+1]}]$ remains unchanged. Finally, by the local support property of B-splines, appending the new control point $\tilde{\mathbf{p}}_{n+1}$ and knot $t_{[n+k+1]}$ affects only the boundary segment, ensuring that the extended curve is identical to the original on $[t_{[0]}, t_{[n+1]}]$ and smoothly extends to $t_{[n+k+1]}$. \square

Example 1. The extension procedure of a cubic C-NUBS ($k = 4$) from $(\mathbf{x}_p, \mathbf{T} = \{0, 0, 0, 0, 1, 2, 3, 3, 3, 3\})$, to $(\mathbf{x}_p'', \mathbf{T}'' = \{0, 0, 0, 0, 1, 2, 3, 4, 4, 4, 4\})$ is illustrated in Fig. 5.

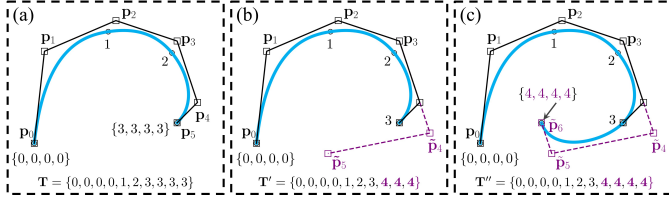


Fig. 5. Closed-form extension of a C-NUBS ($k = 4$). The purple highlights the updated part. $(k - 2)$ control points are adjusted to keep the shape. (a) Original spline. (b) Step 1 and 2 of Proposition 1. (c) Step 3 of Proposition 1.

D. Closed-Form Shrinkage of C-NUBS

Analogous to extension, the shrinkage of a C-NUBS will change its shape. We exploit the knot insertion algorithm [59] and the local support property of B-splines to derive a closed-form shrinkage algorithm.

Proposition 2 (Closed-form shrinkage of a C-NUBS). Consider a C-NUBS curve defined as (4). A shrinkage of this C-NUBS to remove the last interval $[t_{[n]}, t_{[n+1]}]$ is obtained through the following transformation:

- 1) Insert the knot $t_{[n]}$ for $k-1$ times into \mathbf{T} by updated related control points via knot insertion algorithm [59]:

$$\mathbf{T}' : \dots \leq t_{[n]} = \dots = \tilde{t}_{[n+k-1]} \leq t_{[n+1]} = \dots = t_{[n+k]}.$$

- 2) Remove the last k knots and control points and gain:

$$\begin{aligned} \mathbf{x}_p'' &= \{\mathbf{p}_0, \dots, \mathbf{p}_{n-k-1}, \tilde{\mathbf{p}}_{n-k+2}, \dots, \tilde{\mathbf{p}}_{n-1}\}, \\ \mathbf{T}'' &: t_{[0]} = \dots = t_{[k-1]} \leq \dots \leq t_{[n]} = \dots = \tilde{t}_{[n+k-1]}, \end{aligned}$$

The resulting C-NUBS $(\mathbf{x}_p'', \mathbf{T}'')$ is identical to the original curve on $[t_{[0]}, t_{[n+k-1]}]$ and remove the last spline interval. The full algorithm is summarized in Alg. 2.

Algorithm 2 Closed-Form Shrinkage of C-NUBS

Input: A C-NUBS parameterized by $(\mathbf{x}_p, \mathbf{T})$

Output: Shrunk C-NUBS $(\mathbf{x}_p'', \mathbf{T}'')$

- 1: $u \leftarrow T_n$; $s \leftarrow \text{count}_\ell(T_\ell = u)$; $j \leftarrow \max\{\ell \mid T_\ell \leq u\}$.
- 2: **for** $r = 1$ **to** $k - 1$ **do**
- 3: Create a new control set \mathbf{Q} and a new knot vector Υ .
- 4: **for** $i = 0$ **to** $n + 1$ **do**
- 5:
$$\alpha_i = \begin{cases} 1, & i \in [0, j - k + 1] \\ \frac{(u - T_i)}{(T_{i+k-1} - T_i)}, & i \in [j - k + 2, j - s] \\ 0, & i \in [j - s + 1, j + 1] \end{cases}$$
- 6: $\mathbf{Q}_i = \alpha_i \mathbf{p}_i + (1 - \alpha_i) \mathbf{p}_{i-1}$.
- 7: **end for**
- 8: **Insert knot:** $\Upsilon \leftarrow \{T_0, \dots, T_j, u, T_{j+1}, \dots, T_{n+k}\}$.
- 9: **Commit:** $\mathbf{x}_p \leftarrow \mathbf{Q}$, $\mathbf{T} \leftarrow \Upsilon$, $n \leftarrow n + 1$, $s \leftarrow s + 1$.
- 10: $j \leftarrow \max\{\ell \mid T_\ell \leq u\}$.
- 11: **end for**
- 12: Let $\mathbf{x}_p'' \leftarrow \{\mathbf{p}_0, \dots, \mathbf{p}_{n-k}\}$ and $\mathbf{T}'' \leftarrow \{T_0, \dots, T_n\}$.
- 13: **return** \mathbf{x}_p'' , \mathbf{T}'' .

Proof. As shown in [59], inserting a knot into a B-spline can be accomplished by updating the control points using the knot insertion algorithm. By inserting the knot $t_{[n]}$ $k-1$ for times, the resulting knot vector contains the target knot vector of the shrunk spline as a subset. The curve over the original domain $[t_{[0]}, t_{[n+k-1]}]$ remains unchanged after this operation. Finally, removing the last k knots and control points affects only the boundary segment due to the local support property of B-splines, ensuring that the shrunk curve is identical to the original on $[t_{[0]}, t_{[n+k-1]}]$. \square

Example 2. The shrinkage procedure of a cubic C-NUBS ($k = 4$) from $\mathbf{T} = \{0, 0, 0, 0, 1, 2, 3, 3, 3, 3\}$ to $\mathbf{T} = \{0, 0, 0, 0, 1, 2, 2, 2, 2\}$ is illustrated in Fig. 6.

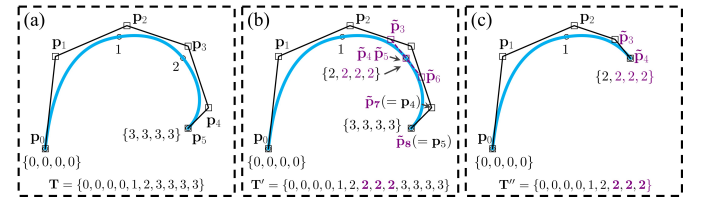


Fig. 6. Closed-form shrinkage of C-NUBS ($k = 4$). The purple highlights the updated part. $(k - 2)$ control points are adjusted to keep the shape. (a) Original spline. (b) Step 1 of Proposition 2. (c) Step 2 of Proposition 2.

E. Generalized to Lie Group

The proposed extension and shrinkage algorithms can be naturally extended to manifolds such as Lie groups. Specifically, by replacing the Euclidean addition in \mathbb{R}^d with Lie group multiplication, and applying appropriate scaling in the Lie algebra through the logarithmic and exponential maps, both the extension and latter shrinkage procedures can be adapted to $SO(3)$ C-NUBS. The control point update in extension Alg. 1(line 9) for $SO(3)$ changes to:

$$\tilde{\mathbf{R}}_i^r = \tilde{\mathbf{R}}_{i-1}^r \cdot \text{Exp} \left(\frac{1}{\alpha_{i,r}} \cdot \text{Log} \left(\left(\tilde{\mathbf{R}}_{i-1}^r \right)^\top \tilde{\mathbf{R}}_i^{r-1} \right) \right), \quad (5)$$

and in shrink Alg. 2(line 6) for $SO(3)$ changes to:

$$\mathbf{Q}_i = \mathbf{R}_{i-1} \text{Exp}(\alpha_i \text{Log}(\mathbf{R}_{i-1}^\top \mathbf{R}_i)). \quad (6)$$

A demonstration of the closed-form extension and shrinkage of a $SO(3)$ C-NUBS is shown in Fig. 7.

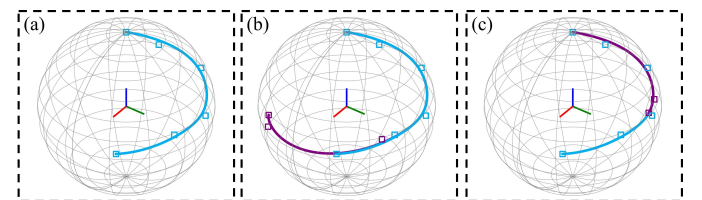


Fig. 7. Example of closed-form extension and shrinkage of $SO(3)$ C-NUBS. The purple highlights the updated part. (a) Original spline. (b) Extended spline. (c) Shrunk spline. $(k - 2)$ control points are adjusted to keep the shape.

F. Knot-Keyknot Strategy for C-NUBS

Most B-spline-based continuous-time state estimation methods are limited by uniformly spaced knots and fixed optimization intervals. In contrast, discrete-time state estimation approaches, such as VINS-Mono [62], adopt a frame–keyframe strategy: performing per-frame optimizations for camera-rate outputs while preserving only informative keyframes in the sliding window to ensure estimation efficiency.

However, such a strategy is difficult to realize with uniform B-splines. Since the knot frequency is typically lower than the measurement rate, producing high-frequency outputs requires extrapolating the spline beyond the latest measurement time t_{last} , resulting in a constraint-free interval before the next knot t_{knot} . Within this interval, the spline evolution relies solely on the inherent smoothness of the B-spline, which leads to degraded observability and potential numerical instability (see Fig. 8). Non-uniform B-splines partially mitigate this issue by allowing knots to be inserted at measurement times, thereby directly constraining the spline tail without extrapolation. Nevertheless, existing unclamped non-uniform formulations suffer from intrinsic query-time delay (as discussed in Sec. III-B).

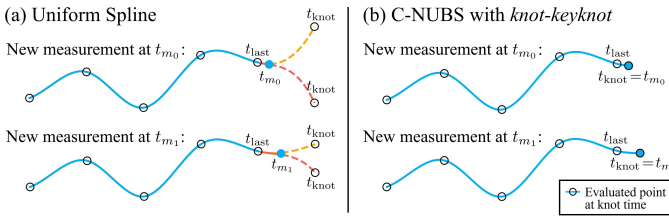


Fig. 8. Tail extrapolation in uniform B-splines and its avoidance using C-NUBS with the knot-keyknot strategy. (a) Uniform knots force tail extrapolation, creating an unconstrained interval that degrades observability and stability. (b) C-NUBS with knot-keyknot inserts a knot at each measurement time, directly constraining the spline tail without extrapolation.

The proposed C-NUBS effectively resolves this limitation by enabling real-time evaluation up to the latest knot while supporting endpoint interpolation. In addition, the proposed extension and shrinkage operations allow flexible manipulation of the terminal knot. Leveraging these properties, we design a *knot-keyknot* strategy for continuous-time state estimation based on C-NUBS, bridging continuous-time spline representations and keyframe-based paradigms.

At each incoming measurement, we extend the B-spline by appending a knot and control point at the measurement timestamp. A sliding-window optimization is then performed over the spline segment span defined by this new knot and existing keyknots. After optimization, if the new knot is not selected as a keyknot, the spline is shrunk back to the last keyknot using closed-form shrinkage, then waits for the next extension. Otherwise, it is retained as keyknot. This process follows an “extend-shift-retain” cycle, as shown in Fig. 8(b).

IV. CONTINUOUS-TIME RELATIVE STATE ESTIMATION PROBLEM FORMULATION

In this section, we formulate a general B-spline-based continuous-time factor graph optimization problem for direct relative localization. This section is not restricted to a specific

B-spline type and supports uniform/non-uniform as well as clamped/unclamped B-splines.

Consider a swarm of n robots indexed by the set $\mathcal{V} = \{0, 1, \dots, n-1\}$, each robot is equipped with an ego-motion sensor (one IMU in this work) and inter-robot sensing (one UWB and one camera in this work). Robots convert raw sensor data into time-stamped observation messages and broadcast them to the team. A designated reference robot s runs the estimator, which jointly estimates inter-robot time-offsets and relative poses from asynchronous measurement streams.

For each robot $j \in \mathcal{V}$, we represent the relative pose with a translation spline ${}^s\mathbf{p}_j(t) \in \mathbb{R}^3$ and a rotation spline ${}^s\mathbf{R}_j(t) \in \text{SO}(3)$. For consistency, the reference robot trajectory is also spline-parameterized, while its pose is anchored by enforcing ${}^s\mathbf{p}_s(t) = \mathbf{0}$ and ${}^s\mathbf{R}_s(t) = \mathbf{I}$. Within the κ -th sliding window $[t_\kappa - \Delta, t_\kappa]$, where Δ denotes the window length, the relative trajectory of robot j is parameterized by active spline control points ${}^s\Phi_j^\kappa$. The estimator optimizes the following state:

$$\begin{aligned} \mathcal{X}^\kappa &= \{ \{ \mathcal{X}_0^\kappa, \mathcal{X}_1^\kappa, \dots, \mathcal{X}_{n-1}^\kappa \}, \Psi^\kappa \}, \\ \mathcal{X}_j^\kappa &= \{ {}^s\Phi_j^\kappa, {}^s\tau_j^\kappa, {}^j\mathbf{b}_a^\kappa, {}^j\mathbf{b}_\omega^\kappa \}, j \in \mathcal{V}. \end{aligned} \quad (7)$$

Here, ${}^s\tau_j^\kappa$ denotes the clock time-offset between robot s and robot j . The vectors ${}^j\mathbf{b}_a^\kappa$ and ${}^j\mathbf{b}_\omega^\kappa$ are the IMU biases of robot j . The auxiliary variable set Ψ^κ collects the control points of an auxiliary IMU spline of the reference robot s . The roles of these variables will be described in the following subsections.

For simplicity, sensor extrinsics are assumed known from offline calibration, following [25], where extrinsics were included in the state but not estimated.

A. Measurement Time-Offset

In CT-RIO, all trajectories are parameterized with respect to the clock of the reference robot s . However, each robot’s measurements are stamped using its own local clock before broadcast. Let ${}^s t$ denote the time of the reference clock of robot s , and ${}^j t$ denote the time of the local clock of robot j . The time-offset between s and j is defined as ${}^s\Gamma_j = {}^s t - {}^j t$.

As illustrated in Fig. 9, using the measurement’s timestamp ${}^j t_m$ instead of its true time ${}^s t_m$ to query on the B-spline and calculate residual can cause error. To compensate for this, we introduce ${}^s\tau_j$ as an optimization variable for robot j . Each measurement’s residual is then calculated by querying the B-spline at the compensated time ${}^s t_m = {}^s\tau_j + {}^j t_m$. By exploiting the analytical gradient of B-spline evaluation with respect to ${}^s t_m$, the offset ${}^s\tau_j$ can be jointly optimized.

For simplicity, in the following text, we use t_c to denote the corrected timestamp, which is obtained by compensating the measurement $\hat{\mathbf{z}}_*$ ’s original timestamp t_m from robot j using the estimated time-offset ${}^s\tau_j$.

B. Inter-Robot Constraints

The relative poses can be queried from the corresponding spline at timestamp t_c as:

$$({}^s\mathbf{R}_j^{t_c}, {}^s\mathbf{p}_j^{t_c}) = {}^s\Phi_j^\kappa|_{t=t_c}. \quad (8)$$

Then, the inter-robot constraints are defined as follows.

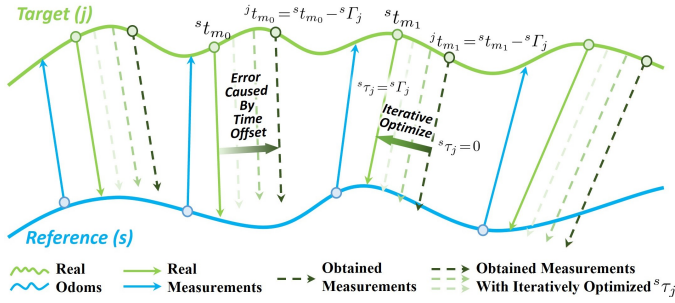


Fig. 9. Illustration of time-offset between the local clock of the target robot and the reference clock, and the correction process of measurement time.

1) *Bearing Factor*: The camera detection model is as:

$$\hat{\mathbf{z}}_{b_{jk}}^t = ({}^s\mathbf{R}_j^t)^\top \frac{{}^s\mathbf{p}_k^t - {}^s\mathbf{p}_j^t}{\|{}^s\mathbf{p}_k^t - {}^s\mathbf{p}_j^t\|_2} + \mathbf{n}_b, \quad (9)$$

where $\mathbf{n}_b \sim \mathcal{N}(0, \Sigma_b)$ is the noise of the bearing vector, j and k are indexes of any two robots. Note that the bearing measurement is a unit vector, which is the normalized vector of the relative position. The residuals can be calculated as:

$$\mathbf{r}_b(\hat{\mathbf{z}}_{b_{jk}}^t, {}^s\tau_j^\kappa, {}^s\Phi_j^\kappa, {}^s\Phi_k^\kappa) = ({}^s\mathbf{R}_j^t)^\top \frac{{}^s\mathbf{p}_k^t - {}^s\mathbf{p}_j^t}{\|{}^s\mathbf{p}_k^t - {}^s\mathbf{p}_j^t\|_2} - \hat{\mathbf{z}}_{b_{jk}}^t. \quad (10)$$

2) *Distance Factor*: The UWB measurement model is as:

$$\hat{\mathbf{z}}_{d_{jk}}^t = \|{}^s\mathbf{p}_k^t - {}^s\mathbf{p}_j^t\|_2 + \mathbf{n}_d, \quad (11)$$

where $\mathbf{n}_d \sim \mathcal{N}(0, \sigma_d^2)$ is the noise of the UWB, j and k are indexes of any two robots. The residuals can be calculated as:

$$\mathbf{r}_d(\hat{\mathbf{z}}_{d_{jk}}^t, {}^s\tau_j^\kappa, {}^s\Phi_j^\kappa, {}^s\Phi_k^\kappa) = \|{}^s\mathbf{p}_k^t - {}^s\mathbf{p}_j^t\|_2 - \hat{\mathbf{z}}_{d_{jk}}^t. \quad (12)$$

C. Motion Constraints

The relative velocities and accelerations can be queried from the corresponding spline at timestamp t_c as:

$$\begin{aligned} ({}^j\boldsymbol{\omega}_{sj}^{t_c}, {}^s\mathbf{v}_{sj}^{t_c}) &= {}^s\dot{\Phi}_j^\kappa|_{t=t_c}, \\ ({}^j\boldsymbol{\beta}_{sj}^{t_c}, {}^s\mathbf{a}_{sj}^{t_c}) &= {}^s\ddot{\Phi}_j^\kappa|_{t=t_c}. \end{aligned} \quad (13)$$

It is worth noting that, for $SO(3)$ B-spline, the derivative is defined in the body frame. The relative motion constraints are then defined as follows.

1) *Relative Kinematics*: We derive the relative motion model in the non-inertial frame s . The relative motion model of robot j in the non-inertial frame s is as follows:

$$\begin{aligned} {}^s\mathbf{a}_{sj} &= \underbrace{-[{}^s\boldsymbol{\beta}_s] \times {}^s\mathbf{p}_j - 2[{}^s\boldsymbol{\omega}_s] \times {}^s\mathbf{v}_{sj} - [{}^s\boldsymbol{\omega}_s]^2 \times {}^s\mathbf{p}_j}_{\text{non-inertial acceleration due to frame rotation}} \\ &\quad + \underbrace{{}^s\mathbf{R}_j^j \mathbf{a}_j - {}^s\mathbf{a}_s}_{\text{linear acceleration}}, \end{aligned} \quad (14)$$

$${}^j\boldsymbol{\omega}_{sj} = {}^j\boldsymbol{\omega}_j - {}^s\mathbf{R}_j^\top {}^s\boldsymbol{\omega}_s, \quad (15)$$

where the gravity components of the measured accelerations are compensated in the linear acceleration term of (14). Additionally, ${}^s\boldsymbol{\beta}_s$ denotes the angular acceleration of reference robot s , which is typically difficult to obtain directly from

IMU measurements. As a result, some existing works assume ${}^s\boldsymbol{\beta}_s = \mathbf{0}$ [63], which inevitably introduces modeling errors. In addition, IMU measurements from robots j and s are generally asynchronous, introducing a time misalignment in (14) and (15). To address both issues, we represent ${}^s\boldsymbol{\omega}_s$ and ${}^s\mathbf{a}_s$ using two \mathbb{R}^3 B-splines, which allowing ${}^s\boldsymbol{\beta}_s$ to be obtained analytically via differentiation, while simultaneously enabling queries of the IMU state from robot s at any time instant.

Specifically, the IMU of reference robot s at timestamp t_m can be queried as:

$$\begin{aligned} ({}^s\boldsymbol{\omega}_s^{t_m}, {}^s\mathbf{a}_s^{t_m}) &= \Psi^\kappa|_{t=t_m}, \\ ({}^s\boldsymbol{\beta}_s^{t_m}, {}^s\dot{\mathbf{a}}_s^{t_m}) &= \dot{\Psi}^\kappa|_{t=t_m}. \end{aligned} \quad (16)$$

2) *IMU Factor*: Due to the nonlinearity of (15), the linearized covariance of ${}^s\mathbf{a}_j$ depends on optimization variables, which may lead to unstable convergence. To ensure correct residual weighting under the Mahalanobis distance and MLE formulation, we introduce the reference robot's two IMU B-splines (${}^s\boldsymbol{\omega}_s$ and ${}^s\mathbf{a}_s$) as auxiliary variables in the optimization, avoiding over-linearization.

The reference robot's IMU residual is defined as:

$$\mathbf{r}_{sIMU}({}^s\hat{\mathbf{a}}_s^{t_m}, {}^s\hat{\boldsymbol{\omega}}_s^{t_m}, \Psi^\kappa) = \begin{bmatrix} {}^s\mathbf{a}_s^{t_m} - {}^s\hat{\mathbf{a}}_s^{t_m} \\ {}^s\boldsymbol{\omega}_s^{t_m} - {}^s\hat{\boldsymbol{\omega}}_s^{t_m} \end{bmatrix}. \quad (17)$$

The relative IMU residual is defined as:

$$\mathbf{r}_i({}^j\hat{\mathbf{a}}_j^{t_m}, {}^j\hat{\boldsymbol{\omega}}_j^{t_m}, {}^s\tau_j^\kappa, {}^s\Phi_j^\kappa) = \begin{bmatrix} \mathbf{r}_{ia} \\ \mathbf{r}_{i\omega} \end{bmatrix}, \quad (18)$$

$$\begin{aligned} \mathbf{r}_{ia} &= -[{}^s\boldsymbol{\beta}_s^{t_c}] \times {}^s\mathbf{p}_j^{t_c} - 2[{}^s\boldsymbol{\omega}_s^{t_c}] \times {}^s\mathbf{v}_{sj}^{t_c} - [{}^s\boldsymbol{\omega}_s^{t_c}]^2 \times {}^s\mathbf{p}_j^{t_c} \\ &\quad + {}^s\mathbf{R}_j^{t_c} {}^j\hat{\mathbf{a}}_j^{t_m} - {}^s\mathbf{a}_s^{t_c} - {}^s\mathbf{a}_j^{t_c}, \end{aligned} \quad (19)$$

$$\mathbf{r}_{i\omega} = {}^j\boldsymbol{\omega}_{sj}^{t_c} - ({}^j\hat{\boldsymbol{\omega}}_j^{t_m} - {}^s\mathbf{R}_j^{t_c \top} {}^s\boldsymbol{\omega}_s^{t_c}), \quad (20)$$

and bias factor based on the random walk process:

$$\mathbf{r}_{ib}({}^j\mathbf{b}_a^\kappa, {}^j\mathbf{b}_\omega^\kappa) = \begin{bmatrix} {}^j\mathbf{b}_a^\kappa - {}^j\mathbf{b}_a^{\kappa-1} \\ {}^j\mathbf{b}_\omega^\kappa - {}^j\mathbf{b}_\omega^{\kappa-1} \end{bmatrix}. \quad (21)$$

D. Marginalization

Since no landmark is used in our system, the marginalization can degenerate into prior constraints of the first states in the sliding window. In CT-RIO, we directly fix the first $k-1$ control points of each robot's B-spline to implement marginalization, as shown in Fig. 10.

E. Full-Batch Optimization Problem Formulation

We formulate the continuous-time relative inertial odometry problem in a factor-graph form. The graph consists of distance factors \mathbf{r}_d , bearing factors \mathbf{r}_b , relative IMU factors \mathbf{r}_i , bias factors \mathbf{r}_{ib} , and auxiliary reference IMU factors \mathbf{r}_{sIMU} , as shown in Fig. 10. To limit the number of optimization variables, we restrict the update of τ_j to the interval $[-\Delta t_j, \Delta t_j]$ per iteration, where Δt_j is the minimum knot interval of robot j 's B-spline. Although this bound enlarges the control-point window from $[t_i, t_{i+k}]$ to $[t_{i-1}, t_{i+k+1}]$, it prevents too much shift in query time that would change the associated control points for each factor. Under this bounded update, τ_j converges to the true value after several successive optimizations. Finally,

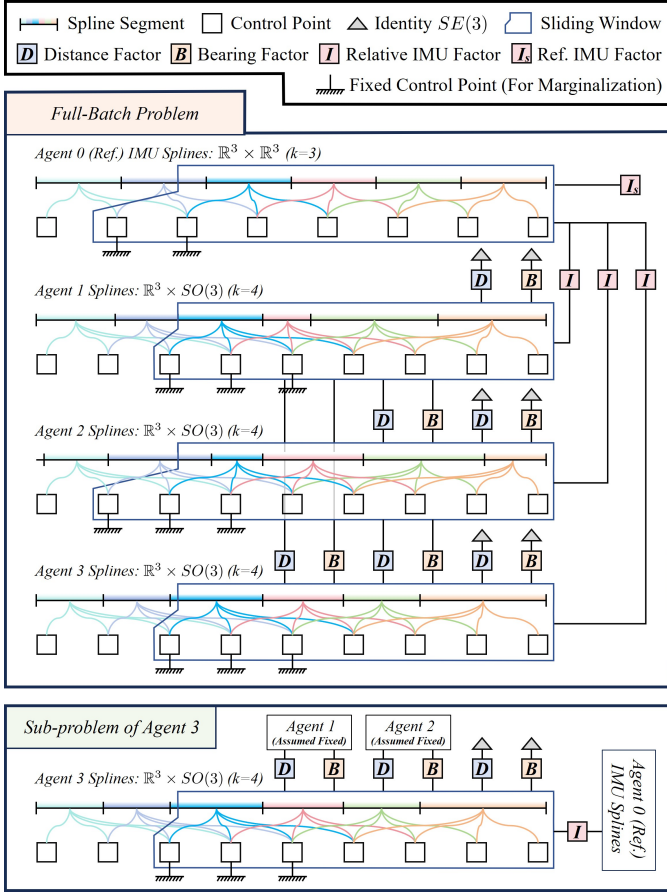


Fig. 10. Factor-graph-like representation of the full-batch problem for a four-robot example, along with one selected subproblem. The state trajectories are parameterized using $k = 4$ B-splines, while the reference robot's IMU are represented using $k = 3$ B-splines. Each trajectory is assembled from individual segments, where each segment depends on a set of control points. A control point remains in the optimization problem as long as any portion of its associated segment lies within the current window.

with the measurements during $[t_\kappa - \Delta, t_\kappa]$, we formulate the following nonlinear least-squares problem:

$$\begin{aligned}
\min_{\mathcal{X}^\kappa} \left\{ \sum_{j \in \mathcal{N}} \sum_{\mathcal{B}_j^{t_m} \in \mathcal{B}_j^\kappa} \sum_{k \in \mathcal{B}_j^{t_m}} \left\| \mathbf{r}_b(\hat{\mathbf{z}}_{jk}^{t_m}, s\tau_j^\kappa, s\Phi_j^\kappa, s\Phi_k^\kappa) \right\|_{\Sigma_b}^2 \right. \\
+ \sum_{j \in \mathcal{N}} \sum_{\mathcal{D}_j^{t_m} \in \mathcal{D}_j^\kappa} \sum_{k \in \mathcal{D}_j^{t_m}} \left\| \mathbf{r}_d(\hat{\mathbf{z}}_{jk}^{t_m}, s\tau_j^\kappa, s\Phi_j^\kappa, s\Phi_k^\kappa) \right\|_{\Sigma_d}^2 \\
+ \sum_{\mathcal{I}_s^{t_m} \in \mathcal{I}_s^\kappa} \left\| \mathbf{r}_{sIMU}(s\hat{\mathbf{a}}_s^{t_m}, s\hat{\boldsymbol{\omega}}_s^{t_m}, \Psi^s) \right\|_{\Sigma_i}^2 \\
+ \sum_{j \in \mathcal{N}} \sum_{\mathcal{I}_j^{t_m} \in \mathcal{I}_j^\kappa} \left\| \mathbf{r}_i(j\hat{\mathbf{a}}_j^{t_m}, j\hat{\boldsymbol{\omega}}_j^{t_m}, s\tau_j^\kappa, s\Phi_j^\kappa) \right\|_{\Sigma_i}^2 \\
\left. + \sum_{j \in \mathcal{N}} \left\| \mathbf{r}_{ib}(j\mathbf{b}_a^\kappa, j\mathbf{b}_\omega^\kappa) \right\|_{\Sigma_{ib}}^2 \right\}. \quad (22)
\end{aligned}$$

We use Levenberg-Marquardt (LM) from Ceres Solver [64] and employ analytical derivatives to solve the problem.

F. Incremental Asynchronous Block Coordinate Descent

The full optimization problem (22) is large-scale and highly nonlinear, especially when the swarm size n is large. To

improve computational efficiency, we simplify the problem and decompose it into smaller components. Specifically, we break the full problem into $n-1$ sub-problems, where each sub-problem involves only the trajectory of a single robot together with its associated factors, as illustrated by the red box in Fig. 10. The reference robot's IMU splines and time-offsets are prefitted and shared across all sub-problems. Formally, each sub-problem is formulated as:

$$\begin{aligned}
\min_{\mathcal{X}_j^\kappa} \left\{ \sum_{\mathcal{B}_j^{t_m} \in \mathcal{B}_j^\kappa} \sum_{k \in \mathcal{B}_j^{t_m}} \left\| \mathbf{r}_b(\hat{\mathbf{z}}_{jk}^{t_m}, s\tau_j^\kappa, s\Phi_j^\kappa, s\Phi_k^\kappa) \right\|_{\Sigma_b}^2 \right. \\
+ \sum_{\mathcal{D}_j^{t_m} \in \mathcal{D}_j^\kappa} \sum_{k \in \mathcal{D}_j^{t_m}} \left\| \mathbf{r}_d(\hat{\mathbf{z}}_{jk}^{t_m}, s\tau_j^\kappa, s\Phi_j^\kappa, s\Phi_k^\kappa) \right\|_{\Sigma_d}^2 \\
+ \sum_{\mathcal{I}_j^{t_m} \in \mathcal{I}_j^\kappa} \left\| \mathbf{r}_i(j\hat{\mathbf{a}}_j^{t_m}, j\hat{\boldsymbol{\omega}}_j^{t_m}, s\tau_j^\kappa, s\Phi_j^\kappa) \right\|_{\Sigma_i}^2 \\
\left. + \left\| \mathbf{r}_{ib}(j\mathbf{b}_a^\kappa, j\mathbf{b}_\omega^\kappa) \right\|_{\Sigma_{ib}}^2 \right\}, \quad (23)
\end{aligned}$$

where $j \in \mathcal{V} \setminus \{s\}$ denotes any non-reference robot.

We solve the sub-problems using an IA-BCD algorithm. IA-BCD has a similar implementation to regular BCD. The difference is that each sub-problem is solved in parallel and asynchronously, without waiting for others to finish and share their updates, but continues to update with the most recent variables available. This greatly improves computational efficiency but also introduces a potential mismatch between the variables used during local optimization and the latest global state. Moreover, the extension/shrinkage of C-NUBS and the incremental growth of residuals and variables change the objective over time, which further affects convergence. We provide convergence analyses in Appendices B and C, showing that despite these inconsistencies, IA-BCD converges to a first-order stationary point of the full problem. In practice, we adopt Ceres' trust-region LM strategy to achieve a balance between numerical stability and convergence speed.

V. CT-RIO IMPLEMENTATION WITH C-NUBS

Tailored to the heterogeneous motion characteristic of robot swarms, we propose a C-NUBS-based continuous-time multi-robot relative inertial odometry framework, CT-RIO, to solve the problem introduced in Sec. IV. We use $k = 4$ C-NUBS to represent robots' trajectories and $k = 3$ unclamped uniform B-splines to represent the reference robot's IMU. The overall pipeline is illustrated in Fig. 11.

At the beginning of the operation or when a new robot joins the network, the uninitialized trajectory is uniformly extended. Then the spline and the time-offset are initialized via full-batch optimization. The full-batch optimization will periodically update the time-offset, as detailed in Sec. V-A.

Once initialization is complete, the related spline is extended at each incoming IMU measurement, with the new control point initialized using relative IMU pre-integration, following Sec. V-B. To reduce redundancy while preserving informative knots, we adopt the *knot-keyknot* strategy to retain only keyknots within the sliding window, based on relative motion intensity as described in Sec. V-C.

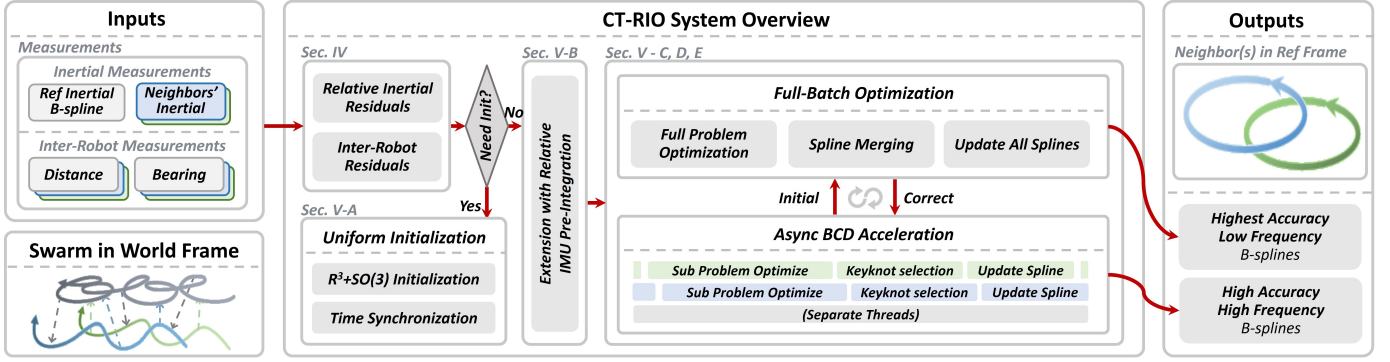


Fig. 11. CT-RIO system overview. The pipeline integrates relative inertial and inter-robot measurements for relative state estimation using C-NUBS. At the beginning, trajectories are uniformly extended and jointly initialized via full-batch optimization. They are then extended at the IMU rate via relative pre-integration with adaptive keyknot selection. Finally, a hybrid optimization scheme is adopted. Asynchronous IA-BCD threads provide high-frequency updates, while periodic full-batch optimization ensures global consistency.

To achieve high-frequency and low-latency updates, a two-layer optimization scheme is adopted. A group of IA-BCD threads continuously optimizes the trajectories by solving the sub-problems (23). Each IA-BCD thread is executed once its corresponding trajectory is extended, providing instant updates at the IMU rate. Meanwhile, a full-batch optimization thread consistently refines the splines to ensure global consistency.

A. System Initialization

At system startup or when a new robot joins the network, the system performs a full-batch optimization to initialize both the spline trajectory and the time-offset.

When a new robot is detected, an initial estimate of the time-offset is obtained via the Network Time Protocol (NTP), with an accuracy of tens of milliseconds [65]. This estimate is incorporated as a prior in the optimization. Then the new robot's trajectory is uniformly extended (10Hz in this paper), and a prior pose sequence from a closed-form single-frame estimator [25] is used to provide an informed initialization.

Then, the full-batch optimization (22) is solved iteratively until the estimated trajectories and time-offsets jointly converge. Since time-offsets drift over long-term operation due to discrepancies in the robot's crystal oscillator, this optimization is periodically re-invoked in a separate thread to continuously refine and update the time-offset. For efficiency, subsequent operations no longer optimize the time-offsets.

B. Extension with IMU Pre-integration Prediction

In this work, we extend the spline at each IMU measurement to ensure IMU-rate output. By leveraging the endpoint interpolation property of clamped B-splines, the target extension control point can be initialized using IMU pre-integration. The IMU pre-integration of a robot in $[t_0, t_1]$ can be calculated as:

$$\begin{aligned} \Delta \mathbf{R}^{t_0 \rightarrow t_1} &= \text{Exp} \left(\int_{t_0}^{t_1} (\hat{\omega}^t - \mathbf{b}_\omega^t) dt \right), \\ \Delta \mathbf{v}^{t_0 \rightarrow t_1} &= \int_{t_0}^{t_1} \Delta \mathbf{R}^{t_0 \rightarrow t} (\hat{\mathbf{a}}^t - \mathbf{b}_a^t) dt, \\ \Delta \mathbf{p}^{t_0 \rightarrow t_1} &= \iint_{t_0}^{t_1} \Delta \mathbf{R}^{t_0 \rightarrow t} (\hat{\mathbf{a}}^t - \mathbf{b}_a^t) dt^2. \end{aligned} \quad (24)$$

With the IMU pre-integration of robot s and j from last keyknot time t_0 to the new knot time t_1 , the target extend control point of robot j ' spline can be calculated as:

$$\begin{aligned} {}^s \mathbf{p}_j^{t_1} &= (\Delta \mathbf{R}_s^{t_0 \rightarrow t_1})^\top \\ &\quad ({}^s \mathbf{p}_j^{t_0} + {}^s \boldsymbol{\mu}_{s_j}^{t_0} \Delta t + {}^s \mathbf{R}_j^{t_0} \Delta \mathbf{p}_j^{t_0 \rightarrow t_1} - \Delta \mathbf{p}_s^{t_0 \rightarrow t_1}), \\ {}^s \mathbf{R}_j^{t_1} &= (\Delta \mathbf{R}_s^{t_0 \rightarrow t_1})^\top ({}^s \mathbf{R}_j^{t_0} \Delta \mathbf{R}_j^{t_0 \rightarrow t_1}), \end{aligned} \quad (25)$$

where ${}^s \boldsymbol{\mu}_{s_j}^{t_0} \triangleq {}^s \mathbf{R}_w^{t_0} {}^w \boldsymbol{\mu}_{s_j}^{t_0} = {}^s \mathbf{v}_{s_j}^{t_0} + {}^s \mathbf{w}_{s_j} \times {}^s \mathbf{p}_j^{t_0}$ is the relative translation velocity between robot s and robot j that does not contain the relative velocity generated by the rotation of robot s . The states ${}^s \mathbf{p}_j^{t_0}$, ${}^s \mathbf{v}_{s_j}^{t_0}$, and ${}^s \mathbf{R}_j^{t_0}$ are evaluated from robot j 's spline at the previous keyknot time t_0 .

Then we use the closed-form extension method in Sec. III-C to extend the spline to this new control point and knot. This provides a reliable starting point for optimization.

C. Relative-Motion-Intensity-Aware Keyknot Strategy

Although the spline is extended to a new knot at every IMU timestamp to support high-rate outputs, only keyknots are retained within the sliding window. Each IA-BCD optimization includes only these keyknots and the new knot. After IA-BCD optimization, we assess whether to promote the new knot as a keyknot based on relative motion. Specifically, we compare the relative states at the new knot time t_1 with those at the last keyknot time t_0 , and apply the following criteria:

- Relative rotation: if $\|\text{Log}({}^s \mathbf{R}_j^{t_0 \top} {}^s \mathbf{R}_j^{t_1})\| > \epsilon_R$, retain the new knot as a keyknot.
- Relative translation: if $\|{}^s \mathbf{p}_j^{t_1} - {}^s \mathbf{p}_j^{t_0}\|_2 > \epsilon_p$, retain the new knot as a keyknot.
- Lower bound: if the time since the last keyframe exceeds $t_{\max} = 200\text{ms}$, retain the new knot as a keyknot.

Where ϵ_R and ϵ_p are thresholds for relative rotation and translation. We empirically set them to $\epsilon_p = 0.08\text{m}$ and $\epsilon_R = 2.5^\circ$ as reference values used throughout all experiments. If the newly added knot is selected as a keyknot, the IMU pre-integration is reset to start from this keyknot, and the next knot can be re-initialized via IMU pre-integration from this keyknot efficiently. This process follows the “extend-shift-retain” cycle in Sec. III-F.

D. Virtual Extension for Optimization

To align the trajectories within the same time window, trajectories that lag behind are *virtually* extended to the latest timestamp with control points set to their most recent IMU-predicted poses, as shown in Fig. 12. After optimization, the *virtual* spline segments are shrunk back to the latest keyknot using closed-form shrinkage and wait for the next extension.

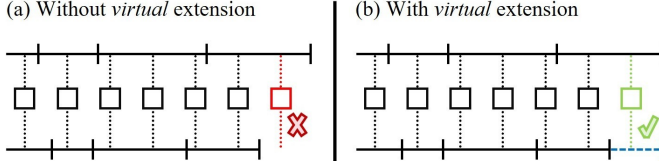


Fig. 12. (a) Without virtual extension, some factors can not be constructed due to the lack of the newest spline segment. (b) With virtual extension, all splines are aligned to the same time window, and all factors can be constructed.

E. Hybrid Optimization Strategy

While the *knot-keyknot* strategy enables outputs at the sensor rate at the constructive level, the actual update frequency remains bounded by the optimization speed. B-spline-based continuous-time estimation suffers from low efficiency due to numerous observations and tightly-coupled control points [30]. This becomes more challenging in CT-RIO because the inter-robot measurements further couple multiple trajectories.

To balance accuracy and efficiency, we adopt a hybrid strategy: Once a spline ${}^s\Phi_j$ is extended, its corresponding sub-problem (23) is immediately optimized. The sub-problems (23) are optimized asynchronously in parallel to allow immediate updates with minimal latency. In this way, IA-BCD locally refines newly introduced control points prior to global fusion, providing better initialization than relying solely on IMU pre-integration. At the same time, a full-batch optimization (22) is consistently triggered in a separate thread as frequently as possible to enforce global consistency through variable synchronization. This corrects the incomplete convergence of IA-BCD, ensuring long-term stability.

After full-batch optimization, the latest trajectory may have been extended several times; thus, beyond updating optimized control points, we merge them with the newly added segments. The continuous trajectory is projected onto anchored poses to preserve local shape, and local linear and angular velocities are sampled from the continuous-time trajectory to constrain its smoothness and ensure coherent merging. The merging procedure can be explicitly formulated as:

$$\begin{aligned} \arg \min_{\Phi^{\text{fused}}} \sum_k & \left(\left\| \text{Log} \left(\hat{\mathbf{R}}_k^\top \mathbf{R}(t_k) \right) \right\| + \left\| \mathbf{p}(t_k) - \hat{\mathbf{p}}_k \right\| \right. \\ & \left. + \left\| \mathbf{R}(t_k)^\top \mathbf{v}(t_k) - \hat{\mathbf{v}}_k \right\| + \left\| \boldsymbol{\omega}(t_k) - \hat{\boldsymbol{\omega}}_k \right\| \right) \\ & + \sum_j \left(\left\| \text{Log} \left(\hat{\mathbf{R}}_j^\top \mathbf{R}(t_j) \right) \right\| + \left\| \mathbf{p}(t_j) - \hat{\mathbf{p}}_j \right\| \right. \\ & \left. + \left\| \mathbf{R}(t_j)^\top \mathbf{v}(t_j) - \hat{\mathbf{v}}_j \right\| + \left\| \boldsymbol{\omega}(t_j) - \hat{\boldsymbol{\omega}}_j \right\| \right), \end{aligned} \quad (26)$$

where variables with hats are sampled from the two result trajectories, the subscript k denotes samples from the full-batch optimization spline, and the subscript j denotes samples from the latest trajectory.

VI. SIMULATION ANALYSIS

To gain deeper insight into the behavior of proposed algorithms, we conduct a series of controlled simulation studies. Overall, our simulation analysis consists of the following parts:

- Sec. VI-B: System-level validation of key components.
- Sec. VI-C: Detailed scalability analysis of the proposed IA-BCD and full-batch optimization.
- Sec. VI-D: Detailed accuracy analysis of the proposed IA-BCD and full-batch optimization.
- Sec. VI-E: Effectiveness analysis of the proposed online time-offset estimation mechanism.

We evaluate the following algorithms:

- **DT**: a discrete-time baseline, corresponding to the MFTO in CREPES-X [25], which achieves the highest accuracy among the four estimators proposed in that work.
- **CT-BCD**: the proposed IA-BCD optimization (23).
- **CT-Full**: the proposed full-batch optimization (22).

and each algorithm has two outputs:

- **Latest Output**: the state evaluated at the latest time of each sliding window from the optimized B-spline.
- **Complete Trajectory**: a global continuous-time trajectory represented by a B-spline after all optimizations.

For clarity, we define the following time-related terms:

- **Run time**: build time + solve time.
- **Latency**: run time + modeling-introduced delay.
- **Time-Offset**: clock time-offset between robots.
- **Output Frequency**: the frequency of output, limited by the maximum value of “build time” and “solve time”.

A. Simulation Setup

We generate random 6-order $SE(3)$ B-splines to simulate the trajectories. The knot interval of the B-spline is set to 1 second. The position control points are sampled uniformly within a cube of size $10 \times 10 \times 10m^3$ space, while the rotation control points are generated following [66]. Mutual measurements are generated by sampling positions and rotations along the trajectory. IMU measurements are derived from the derivatives of the B-spline. Gaussian noise is manually added to measurements, specified in Tab. II.

TABLE II: SIMULATION CONFIGURATION

Metric	Bearing	Distance	IMU	
			Acc.	Gyro.
Frequency	50 Hz	100 Hz	100 Hz	100 Hz
Noise [σ]	2.00°	0.10 m	0.10 m/s ²	0.01 rad/s

All experiments selected Device 0 as the reference device, estimating the relative poses of other devices with respect to it. Following the evaluation protocol in [67], we compute the Absolute Trajectory Error (ATE) of the estimated relative poses in the local frame of Device $s = 0$. For a sequence of M outputs of N other devices, the ATE is computed as:

$$\begin{aligned} \text{ATE}_R &= \sqrt{\frac{1}{M} \sum_{i=1}^M \frac{1}{N} \sum_{j=1}^N \left\| \left\langle \mathbf{R}_s^{t_i}{}^\top \mathbf{R}_j^{t_i} \hat{\mathbf{R}}_j^{t_i}{}^\top \right\rangle \right\|^2}, \\ \text{ATE}_p &= \sqrt{\frac{1}{M} \sum_{i=1}^M \frac{1}{N} \sum_{j=1}^N \left\| \mathbf{R}_s^{t_i}{}^\top (\mathbf{p}_j^{t_i} - \mathbf{p}_s^{t_i}) - \hat{\mathbf{p}}_j^{t_i} \right\|^2}. \end{aligned}$$

All experiments are conducted on a computer equipped with an Intel i5-1260P CPU and 8 GB of RAM.

B. System-Level Validation of Key Components

To validate the impact of individual components on system performance, we conduct a comprehensive ablation study using 8 devices, with the results summarized in Tab. III. This serves as the foundation for more detailed analyses in subsequent sections.

TABLE III: ABLATION STUDY OF DIFFERENT COMPONENTS

Methods	Frequency	Latency	RMSE
1 Discrete-Time (10 Hz keyframe)	10.0 Hz	14.4 ms	0.026 m
2 Continuous-Time (Unclamped, 10 Hz knot)	10.0 Hz	280.2 ms	0.010 m
3 + Clamped (10 Hz knot)	10.0 Hz	79.7 ms	0.010 m
4 + Clamped + <i>knot-keyknot</i>	12.5 Hz	78.6 ms	0.010 m
5 + Clamped + <i>knot-keyknot</i> + IA-BCD	100.0 Hz	7.0 ms	0.010 m

We first compare the DT formulation with the CT formulations (rows 1-2 of Tab. III). Both the knot spacing of CT and the keyframe spacing of DT are set to 100 ms, and the optimization frequency is fixed at 10 Hz using full-batch optimization. While DT achieves relatively low output latency, its estimation accuracy is substantially worse than that of all CT methods. A simple quantitative assessment reveals that, at a 100 ms keyframe interval, DT discards approximately 80% of bearing and 90% of distance measurements, with IMU data downsampled through pre-integration. This exposes a key limitation of DT formulation: under fixed keyframe spacing, low latency is achieved by discarding a large fraction of high-rate measurements, leading to degraded accuracy. In contrast, CT formulations naturally incorporate asynchronous and high-frequency measurements without such information loss.

We then compare unclamped and clamped CT formulations (rows 2-3 of Tab. III) under equal conditions, constraining the keyknot and optimization frequency at 10 Hz with only full-batch optimization. Both configurations achieve identical output RMSE, confirming the theoretical analysis that clamping does not reduce the approximation capability of B-splines. Furthermore, clamping significantly reduces output latency from 280.2 ms to 79.7 ms by eliminating the intrinsic query-time delay (200 ms when $k = 4$ and knot spacing is 100 ms), enabling direct state evaluation at the latest measurement time.

Finally, we evaluate the CT-RIO system, which incorporates clamped, *knot-keyknot*, and IA-BCD optimization. The full-batch optimization (clamped with *knot-keyknot* coupling, row 4 of Tab. III) maintains the output frequency at 12.5 Hz and latency at 78.6 ms, as the output frequency is constrained by the optimization time. Employing the proposed IA-BCD scheme (row 5 of Tab. III) significantly increases the output frequency to 100 Hz and reduces the output latency to 7.0 ms.

Notably, all CT configurations achieve the same output RMSE, indicating that the improvements in frequency and latency are obtained without sacrificing estimation accuracy. These results demonstrate that clamping primarily addresses intrinsic modeling-induced latency, while IA-BCD enables high-frequency, low-latency state updates at the system level, making CT-RIO outperform other formulations across all metrics. A visualization of the results is provided in Fig. 3.

C. Scalability Analysis

To evaluate the scalability of the proposed CT optimization algorithms, we analyze their runtime behavior under varying numbers of robots and time-window sizes, and compare them against the DT baseline. Fig. 13 summarizes the results.

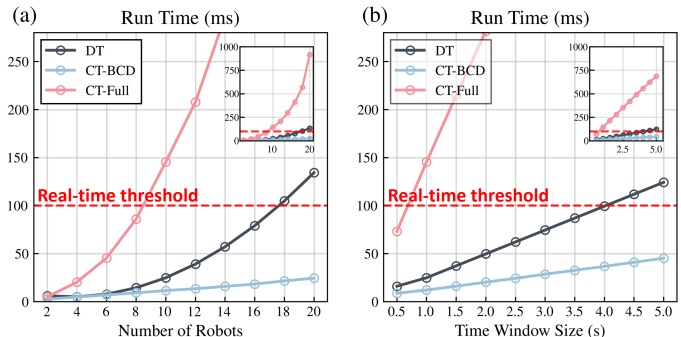


Fig. 13. Scalability analysis of DT, CT-BCD, and CT-Full. Run time versus (a) the number of robots with a fixed 1 s time window, and (b) the time window size with 10 robots.

Fig. 13 (a) shows that DT exhibits exponential runtime growth with the increase of the number of devices, surpassing the real-time threshold (100 ms) at around 18 devices. CT-Full also grows exponentially, exceeding real-time constraints at about 10 devices and rising sharply to approach 1 s once the device count exceeds 20. In contrast, CT-BCD scales linearly and consistently remains below 25 ms even with 20 devices, making it the only algorithm suitable for large-scale real-time deployment. With respect to time-window size, all three methods exhibit linear runtime growth, as illustrated in Fig. 13 (b). Despite linear complexity, CT-Full’s large baseline runtime prevents real-time operation even with a 1 s window.

TABLE IV: TOTAL PROCESSING TIME IN MILLISECONDS (ms)

Window	DT		CT-BCD		CT-Full	
	Build	Solve	Build Stand. / Incr.	Solve	Build Stand. / Incr.	Solve
1s	3.0	20.2	6.8 / 3.2	8.7	18.3 / 11.1	134.4
3s	8.7	57.3	18.9 / 3.1	25.2	53.4 / 11.1	409.8
5s	14.4	102.8	31.7 / 3.1	41.9	91.2 / 11.1	674.5

We further analyze the composition of run time using 10 devices, as shown in Tab. IV. For a fair comparison with DT, we present the time taken by CT methods to reconstruct the optimization problem in Ceres [64] from scratch each time (column “Standard” of Tab. IV), consistent with DT and other Ceres-based methods. DT discards part of the observations and requires less time for problem construction, and also its weaker variable coupling leads to a shorter solving time compared with CT-Full. Since all measurements are included in the optimization, CT-Full exhibits significantly higher construction and solving times than the other methods. Meanwhile, CT-BCD achieves a lower construction time than CT-Full and the lowest solving time due to its block-wise strategy.

However, reconstructing the optimization problem each time is computationally expensive and can even approach the solving time in CT-BCD. Therefore, we implement an incremental problem construction strategy for CT methods and report its effect in Tab. IV (column “Incremental”). This strategy

updates only the parts that change between optimizations by adding newly introduced variables and factors and removing marginalized ones. As a result, the problem construction time for CT methods is significantly reduced and becomes nearly constant with respect to the time window size, which is particularly advantageous for large-window scenarios.

D. Accuracy Analysis

In this section, we analyze the performance of IA-BCD and full-batch optimization to characterize their accuracy and clarify the motivation for the Hybrid strategy. To enable a controlled comparison, we isolate the IA-BCD and Full-Batch components from the Hybrid strategy (see Sec. V-E), constructing IA-BCD-Only and Full-Batch-Only variants, and compare them with DT. The corresponding outputs are denoted as CT-BCD_(H), CT-Full_(H), CT-BCD_(I), and CT-Full_(F).

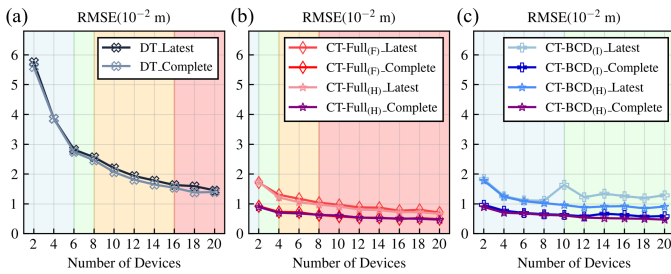


Fig. 14. RMSE of different CT optimization strategies and DT versus the number of robots, with a fixed 1 s time window. Background colors indicate real-time capability: **Blue**: IMU-rate (< 10 ms); **Green**: Camera-rate (< 20 ms); **Yellow**: Real-time (< 100 ms); **Red**: Non-real-time (> 100 ms).

1) *Full-Batch-Only*: As shown in Fig. 14, CT-Full_(F) consistently achieves the lowest error, with estimation accuracy improving monotonically as the number of robots increases. Meanwhile, the accuracy of the complete trajectory is consistently higher than that of the latest output. This behavior contrasts with DT, where the complete trajectory does not exhibit comparable improvements. We attribute this gap to differences in measurement time alignment: DT usually requires measurement interpolation or discarding, which limits information utilization and attainable accuracy, whereas CT-Full_(F) evaluates all measurements at their original timestamps, providing substantially richer constraints. In addition, CT-Full_(F) effectively leverages accumulated historical information to further improve complete trajectory accuracy by refining intermediate states using temporal context. However, due to its tightly-coupled optimization structure, CT-Full_(F) shows significantly poorer real-time scalability than DT, as indicated by the background colors in Fig. 14(a)(b).

2) *IA-BCD-Only*: In IA-BCD-Only strategy, CT-BCD_(I) exhibits significantly different behavior compared to CT-Full_(F). As shown in Fig. 14(c), for the latest output, the estimation error initially decreases as the number of robots increases, but begins to rise once the number of robots exceeds 10. Meanwhile, the solver can no longer perform optimization at every extension step when beyond 10 robots, as shown in the background color of Fig. 14(c). This suggests that fewer optimization updates limit the convergence of CT-BCD_(I). For the complete trajectory, each variable undergoes more

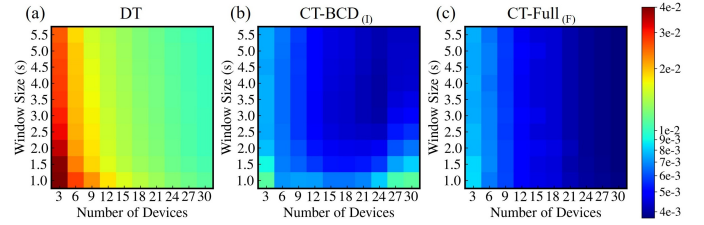


Fig. 15. RMSE comparison of CT optimization strategies and DT under fixed update rates, evaluated across varying numbers of robots and time window sizes. Each column denotes to a specific method. The top row shows the latest-output RMSE, and the bottom row shows the complete-trajectory RMSE.

subproblem optimization iterations. As a result, CT-BCD_(I) is able to converge to an accuracy comparable to CT-Full_(F) when a sufficient number of iterations is allowed.

To further analyze this effect, we eliminate the influence of varying computation times by running all methods at fixed rates (100 Hz for IA-BCD and 10 Hz for Full-Batch and DT) and increasing the time window size up to 5.5 s. Under fixed rates, a larger window effectively provides each variable with more optimization updates, allowing us to analyze convergence behavior. As shown in Fig. 15(b)(c), as the number of devices increases, the iterations required by CT-BCD_(I) to reach an accuracy comparable to CT-Full_(F) grow significantly. This trend indicates that although IA-BCD also benefits from the richer information of a larger swarm, its convergence slows due to the increased problem scale and weaker coupling to the global objective. Despite this limitation, CT-BCD_(I) demonstrates superior real-time scalability compared to other methods, as illustrated by the background colors in Fig. 14(c).

3) *Hybrid*: For the latest output, periodic full-batch refinements accelerate the convergence of CT-BCD by globally correcting the trajectory. As shown in Fig. 14(c), this allows CT-BCD_(H) to achieve accuracy close to CT-Full_(H) (Fig. 14(b)) and significantly outperform standalone CT-BCD_(I). Meanwhile, the CT-Full_(H) consistently maintains its high accuracy. For the complete trajectory, the Hybrid strategy achieves accuracy that closely matches pure full-batch optimization. Overall, the Hybrid strategy inherits the fast global convergence and high accuracy of full-batch optimization, while leveraging the computational efficiency of IA-BCD for real-time updates.

E. Time-Offset Estimation Analysis

This experiment evaluates the effectiveness and robustness of the proposed time-offset estimation mechanism under varying levels of inter-device clock misalignment. We construct a controlled benchmark by artificially adding additional time-offsets of each device in the simulation spline. For a given time-offset magnitude, the time-offsets are distributed uniformly within the range to emulate realistic clock discrepancies, as shown in the start of Fig. 16.

Tab. V reports the position RMSE of DT and CT-Full, together with the time-offset estimation error and the number of optimization steps required for convergence. Each step corresponds to a complete full-batch optimization, in which the time-offset variable τ is jointly updated within the bounded interval $[-\Delta t_j, \Delta t_j]$, as formulated in Sec. IV-E. When no time-offset is introduced, CT-Full consistently achieves lower

TABLE V: TIME-OFFSET ESTIMATION ACCURACY AND RMSE OF DT AND CT-FULL UNDER DIFFERENT TIME-OFFSET SETTINGS

Time-Offset (ms)	Num of Devices	Window Size (s)	DT				CT-Full with τ Estimation	
			RMSE (m)	RMSE (m)	Esti. τ Error (ms)	Steps		
0	2	1.0	0.050	0.014	-2.63 ± 2.69	1		
		3.0	0.037	0.011	-1.26 ± 1.39	1		
		5.0	0.037	0.010	-0.40 ± 1.12	1		
	5	1.0	0.032	0.009	0.04 ± 1.30	1		
		3.0	0.026	0.009	-0.22 ± 0.55	1		
		5.0	0.027	0.009	-0.27 ± 0.40	1		
100	2	1.0	0.206	0.011	-2.78 ± 3.11	12		
		3.0	0.259	0.011	-1.31 ± 1.35	2		
		5.0	0.292	0.010	-0.42 ± 1.13	2		
	5	1.0	0.184	0.009	-0.05 ± 1.28	6		
		3.0	0.195	0.008	-0.23 ± 0.56	2		
		5.0	0.197	0.009	-0.26 ± 0.40	2		
1000	2	1.0	3.385	0.014	-1.09 ± 3.45	34		
		3.0	3.425	0.010	0.27 ± 0.37	27		
		5.0	3.492	0.011	0.40 ± 0.34	20		
	5	1.0	2.093	0.009	-0.17 ± 1.59	29		
		3.0	2.208	0.009	-0.15 ± 0.71	27		
		5.0	2.149	0.009	-0.03 ± 0.37	28		

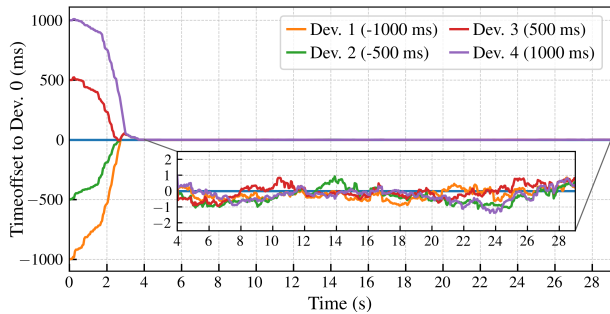


Fig. 16. Time-offset estimation results of five devices under 5 s sliding time window in the benchmark.

RMSE than DT across all window sizes and numbers of devices. Meanwhile, the estimated time-offset remains tightly concentrated around zero with small variance, indicating that the introduction of time-offset variables does not induce bias or instability in the nominal synchronized setting.

As the time-offset increases to 100 ms, DT exhibits significant performance degradation due to temporal misalignment, whereas CT-Full maintains stable accuracy with RMSE comparable to the zero-offset case. The estimated time-offset converges to the ground truth with a millisecond mean error, indicating reliable temporal calibration. Under severe time-offsets of 1000 ms, DT fails completely with meter-level RMSE, while CT-Full consistently achieves accurate estimation, keeping RMSE below 0.014 m. Although larger time-offsets require more optimization steps due to bounded ranges, the final accuracy of CT-Full is not compromised. Fig. 16 illustrates the time-offset estimation process of the five devices using a 5 s sliding time window. The time-offsets converge within the first 4 s and remain stable for the remaining time. Meanwhile, larger window sizes and more devices improve the stability and convergence of time-offset estimation by providing richer constraints and redundancy, demonstrating the robustness and scalability of the proposed continuous-time formulation with joint time-offset estimation.

VII. REAL-WORLD EXPERIMENTS

In this section, we evaluate the CT-RIO from multiple perspectives through real-world experiments. First, we compare its pose estimation accuracy against the discrete-time estimator CREPES-X-MFTO [25]. Next, we systematically analyze the accuracy and necessity of online time-offset estimation. Finally, we examine the performance differences between non-uniform and uniform B-spline knot placements.

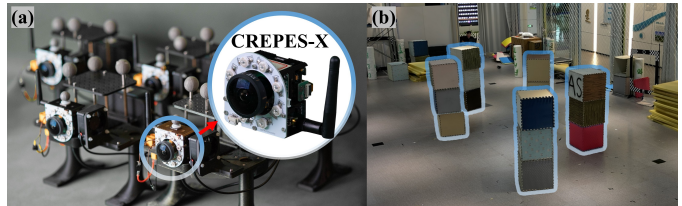


Fig. 17. The experiment environment and the platform. (a) The platform of CREPES-X [25] devices. (b) The environment of NLOS conditions.

The experiments are conducted indoors using five hand-held CREPES-X [25] devices, as shown in Fig. 17(a). The experiments cover diverse motion patterns with varying linear and angular velocities, include heterogeneous motions across different devices, and encompass both Line-of-Sight (LOS) and Non-Line-of-Sight (NLOS) conditions. In LOS experiments, the environment remains unobstructed. In NLOS experiments, obstacles are randomly placed to obstruct mutual observations, as illustrated in Fig. 17(b). A ground of dedicated time-offset experiments is additionally designed to evaluate CT-RIO's online time-offset estimation performance. Ground-truth poses are provided by a motion-capture system, and the sensor extrinsics are calibrated following the procedure in [25]. All experiments are organized into the following four types based on the motion patterns and time-offset configurations:

- **Smooth Motion:** All devices traverse and return within a $10 \times 20 \times 3 \text{ m}^3$ space with gentle and continuous motions, including **LOS** and **NLOS** sequences.
- **Shift-Speed Motion:** One device moves with a time-varying velocity profile, alternating between faster and slower motions, while all other devices (including Device 0) remain stationary in LOS conditions, including Shift-speed Dynamic Motion (**SDM**) sequences.
- **High-Speed Motion:** Two devices (including Device 0) in LOS and NLOS conditions are manually swung at high speed, while the remaining three stay stationary, creating aggressive relative motions, including High-speed Dynamic Motion (**HDM**) sequences.
- **Time-offset Unsynchronization:** All devices traverse and return within a $10 \times 20 \times 3 \text{ m}^3$ space in LOS conditions, including Time-offset UnSynchronized (**TUS**) sequences. The UWB time synchronization is disabled and just relies on Wi-Fi for time synchronization, which has an accuracy of around tens of milliseconds [27]. The ground truth time-offsets are obtained via wired clock synchronization with sub-millisecond precision.

The corresponding sensor noise levels are summarized in Tab. VII for reference.

TABLE VI: REAL-WORLD EXPERIMENT STATISTICS AND RMSE OF DT AND CT (LATEST OUTPUT, COLOR DEFINITION: **BEST**, **SECOND-BEST**, DETERMINED BY POSITION RMSE, AND BY ROTATION RMSE IF EQUAL)

Experiment	Avg. Length (m)	Avg. Time (s)	Avg. Velocity (m/s)	Avg. Angular Velocity (°/s)	Avg. Relative Velocity (m/s)	Avg. Relative Angular Velocity (°/s)	E_{DT}		E_{CT-BCD} (IA-BCD-Only)		E_{CT-BCD} (Hybrid)		$E_{CT-Full}$ (Hybrid)		$\left \frac{E_{DT} - E_{CT-Full}}{E_{DT}} \right $ %	
							Pos (m)	Rot (°)	Pos (m)	Rot (°)	Pos (m)	Rot (°)	Pos (m)	Rot (°)	Pos	Rot
Smooth	LOS_1	20.484	61.632	0.332	16.198	0.997	24.177	0.063 / 1.931	0.060 / 1.878	0.058 / 1.885	0.058 / 1.879	8%↑	3%↑			
	LOS_2	19.646	36.695	0.535	19.768	1.202	29.482	0.078 / 2.088	0.074 / 2.003	0.070 / 1.992	0.069 / 2.008	12%↑	4%↑			
	LOS_3	19.649	35.126	0.559	20.624	0.980	26.586	0.069 / 2.107	0.063 / 2.018	0.062 / 2.017	0.061 / 2.065	12%↑	2%↑			
	LOS_4	20.813	21.660	0.961	25.353	1.009	31.415	0.080 / 2.538	0.072 / 2.479	0.070 / 2.438	0.070 / 2.417	12%↑	5%↑			
	NLOS_1	21.349	54.860	0.389	14.898	0.508	16.920	0.050 / 1.836	0.074 / 1.815	0.047 / 1.829	0.046 / 1.823	8%↑	1%↑			
	NLOS_2	21.570	34.780	0.620	18.979	0.643	21.450	0.067 / 1.997	0.111 / 1.979	0.058 / 1.980	0.055 / 1.977	18%↑	1%↑			
	NLOS_3	21.226	32.570	0.652	20.649	0.770	24.518	0.059 / 1.997	0.093 / 1.978	0.056 / 1.982	0.055 / 1.989	7%↑	0%↑			
	NLOS_4	21.119	23.220	0.910	24.174	0.835	26.999	0.070 / 2.095	0.073 / 2.066	0.063 / 2.079	0.061 / 2.092	13%↑	0%↑			
Shift-Speed	SDM_1	56.496	65.130	0.867	85.165	1.015	85.191	0.067 / 2.526	0.060 / 2.285	0.053 / 2.449	0.051 / 2.468	24%↑	2%↑			
	SDM_2	43.491	60.591	0.718	62.238	0.823	62.281	0.053 / 1.837	0.049 / 1.943	0.047 / 1.791	0.045 / 1.817	15%↑	0%↑			
	SDM_3	45.965	63.549	0.723	74.407	0.837	74.407	0.068 / 2.702	0.052 / 2.520	0.048 / 2.593	0.046 / 2.594	32%↑	4%↑			
	SDM_4	44.571	51.903	0.859	73.187	0.972	73.207	0.064 / 2.125	0.050 / 2.206	0.049 / 2.089	0.047 / 2.093	27%↑	2%↑			
High-Speed	HDM_1	56.206	25.970	2.164	186.849	10.006	213.379	0.239 / 2.715	0.277 / 3.104	0.194 / 2.533	0.179 / 2.523	25%↑	7%↑			
	HDM_2	35.401	24.971	1.418	94.830	8.147	118.162	0.171 / 2.122	0.193 / 2.555	0.140 / 2.140	0.120 / 1.901	30%↑	10%↑			
	HDM_3	29.027	18.970	1.530	116.546	7.962	150.436	0.205 / 2.611	0.145 / 2.705	0.115 / 2.356	0.106 / 1.913	48%↑	27%↑			
	HDM_4	44.133	28.976	1.523	108.897	7.351	135.181	0.182 / 2.645	0.196 / 2.587	0.146 / 2.252	0.133 / 2.072	27%↑	22%↑			

TABLE VII: EXPERIMENT CONFIGURATION

Metric	Bearing	Distance	IMU	
			Acc.	Gyro.
Frequency	50 Hz	100 Hz	100 Hz	100 Hz
LOS Noise [σ]	3.661°	0.055 m	1.946 m/s ²	12.226°/s
NLOS Noise [σ]	3.263°	0.057 m	2.062 m/s ²	12.492°/s
SDM Noise [σ]	5.145°	0.046 m	1.967 m/s ²	16.235°/s
HDM Noise [σ]	2.892°	0.107 m	0.895 m/s ²	10.353°/s
TUS Noise [σ]	1.571°	0.129 m	1.162 m/s ²	15.508°/s

The experimental evaluation consists of the following three parts:

- Sec. VII-A: Comparison of the CT and the DT estimators in **LOS**, **NLOS**, **SDM**, and **HDM** sequences.
- Sec. VII-B: Accuracy and necessity of online time-offset estimation in **TUS** sequences.
- Sec. VII-C: Comparison of non-uniform and uniform knot frequency in **LOS**, **NLOS**, **SDM**, and **HDM** sequences.

A. Comparison of Continuous-Time and Discrete-Time

We compare the pose estimation accuracy of CT-RIO against DT on all experiments except **TUS**. For CT-RIO, similar to Sec. VI-D, we evaluate CT-BCD under the IA-BCD-only strategy (CT-BCD_(I)), and both CT-BCD and CT-Full under the Hybrid strategy (CT-BCD_(H) and CT-Full_(H)). The Full-Batch-Only strategy is omitted, as benchmark results indicate only marginal performance differences compared to the Hybrid strategy. The time window for both CT-RIO and DT is set to 3s. The RMSE in **SDM** and **HDM** are computed only for the moving device (Device 1), and the statistical data include only Device 1 and Device 0.

1) *Latest Output*: Results are summarized in Tab. VI. CT-RIO in the Hybrid strategy consistently outperforms DT across all experiments. In smooth motion scenarios, CT-Full_(H) achieves modest improvements of 7% ~ 18% in position accuracy, suggesting that DT methods already perform competitively under favorable motion conditions. In shift-speed

motion scenarios, CT-Full_(H) achieves 15% ~ 32% gains in position accuracy. In high-speed motion scenarios, CT-Full_(H) demonstrates substantial advantages, achieving 25%–48% improvements in position accuracy over DT, which highlights the effectiveness of continuous-time modeling in handling rapid motion and highly asynchronous observations. In terms of rotation, CT-Full_(H) shows negligible improvements in smooth and shift-speed motion scenarios, but delivers notable gains in high-speed motion scenarios, with improvements of up to 27%. This can be attributed to the fact that low-frequency measurements suffice to constrain rotation errors in smooth and shift-speed scenarios, whereas in high-speed scenarios, CT-RIO benefits from integrating constraints at precise timestamps, significantly enhancing rotation estimation accuracy.

Across different CT-RIO strategies, consistent performance trends are observed among CT-BCD_(I), CT-BCD_(H), and CT-Full_(H), with estimation errors decreasing in that order. CT-BCD_(H) achieves comparable performance to CT-Full_(H) in smooth and shift-speed motion scenarios, and only slightly lags behind in high-speed motion scenarios. Meanwhile, CT-BCD_(I) exhibits a more pronounced performance gap relative to CT-Full_(H). Under well-conditioned **LOS** and **SDM** scenarios, CT-BCD_(I) still outperforms DT. However, in challenging **NLOS** and **HDM** scenarios, its performance degrades significantly, and can even fall below that of DT. This behavior indicates that instant robot-wise BCD updates are sensitive to observation quality, whereas the Hybrid strategy effectively mitigates this limitation by incorporating full-batch updates. Noting that CT-BCD_(H) can output at IMU-frequency, these results highlight the advantages of the Hybrid strategy in delivering high-accuracy, low-latency, and high-frequency outputs.

2) *Complete Trajectory*: The results are summarized in Tab. VIII. In the Hybrid strategy, CT-BCD_(H) and CT-Full_(H) share the same complete trajectory, so only CT-Full_(H) is reported. Overall, estimation accuracy improves consistently from DT to CT-BCD_(I), and further to CT-Full_(H). Compared

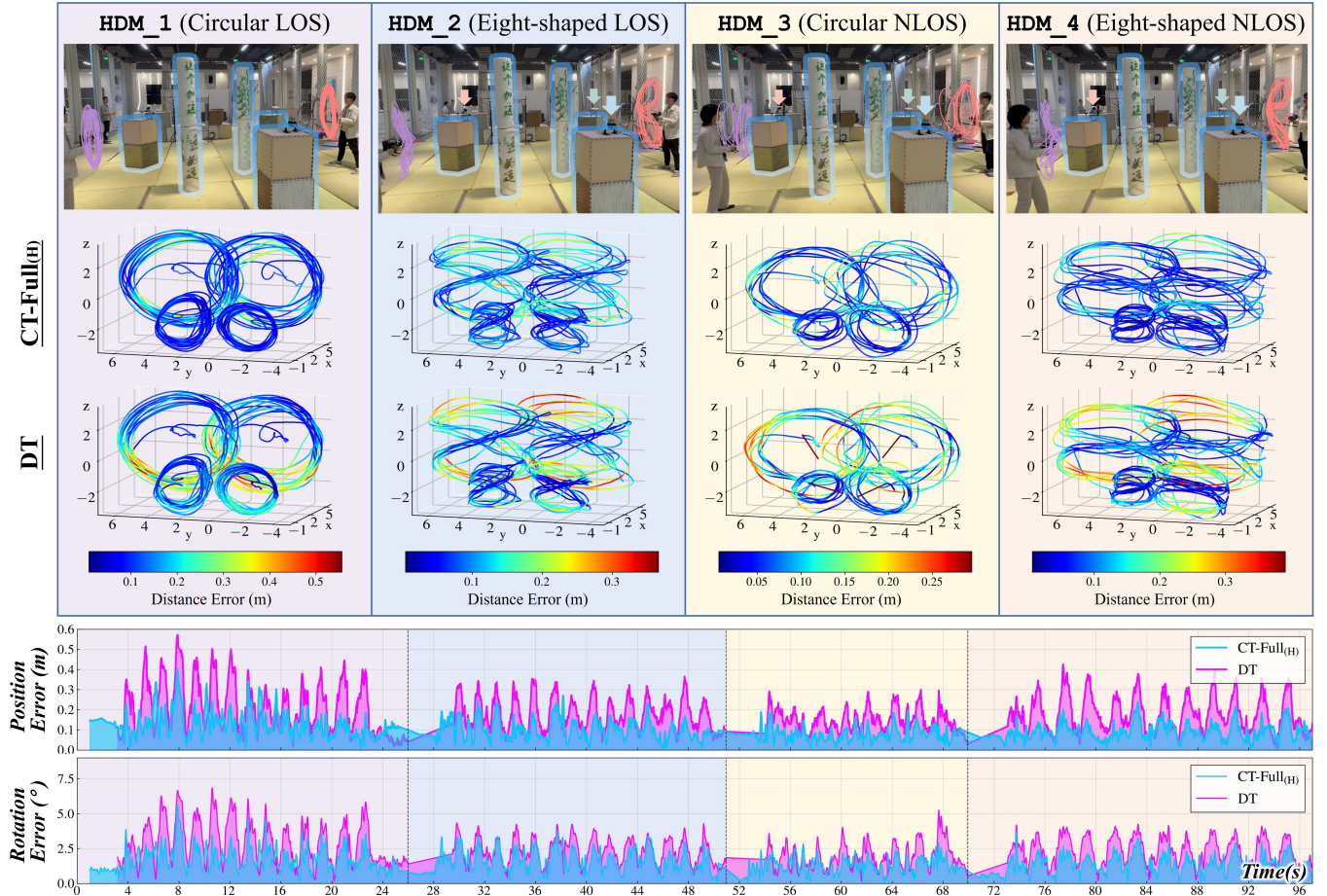


Fig. 18. High dynamic motion (HDM) results. Upper: Trajectories in world frame and the estimated outputs in reference frame (Device 0) by CT (CT-Full_(H)) and DT (CREPES-X-MFTO), respectively. Lower: Position and rotation errors of Device 1.

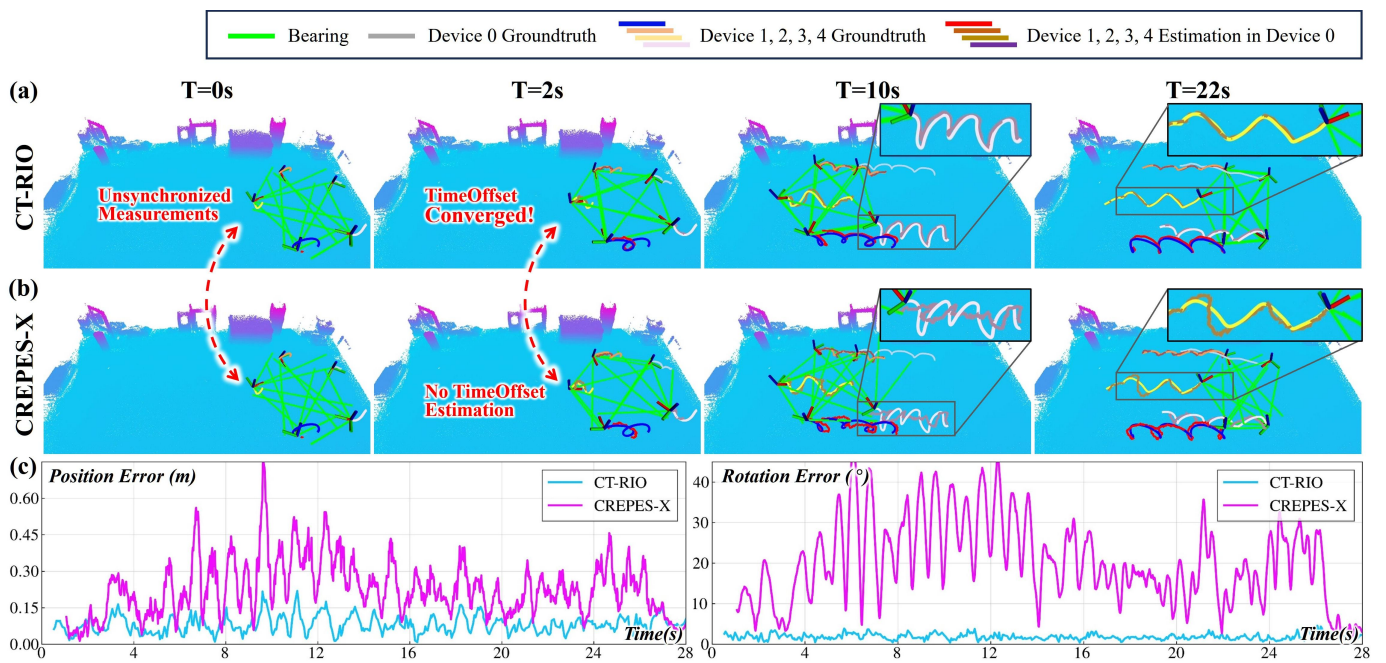


Fig. 19. Results of online time-offset estimation in TUS_1. The estimated relative trajectories are transformed to the world frame. (a) CT (CT-RIO) outputs with online time-offset estimation. (b) DT (CREPES-X) outputs without time-offset estimation. (c) Position and rotation errors of device 4 (reference frame is device 0). The errors spike in DT due to the uncorrected time-offsets.

TABLE VIII: RMSE OF DT AND CT IN REAL-WORLD EXPERIMENT (COMPLETE TRAJECTORY, COLOR DEFINITION: BEST, SECOND-BEST, DETERMINED BY POSITION RMSE, AND BY ROTATION RMSE IF EQUAL)

Experiment	E_{DT}		E_{CT-BCD} (IA-BCD-Only)		$E_{CT-Full}$ (Hybrid)		$\frac{ E_{DT} - E_{CT-Full} }{E_{DT}}$ %	
	Pos	Rot	Pos	Rot	Pos	Rot	Pos	Rot
	(m)	(°)	(m)	(°)	(m)	(°)		
LOS_1	0.062 / 1.935		0.054 / 1.795		0.054 / 1.788		13%↑	8%↑
LOS_2	0.077 / 2.081		0.065 / 1.983		0.065 / 1.943		16%↑	7%↑
LOS_3	0.068 / 2.117		0.058 / 2.030		0.057 / 2.052		16%↑	3%↑
LOS_4	0.078 / 2.517		0.066 / 2.521		0.065 / 2.434		17%↑	3%↑
NLOS_1	0.050 / 1.840		0.049 / 1.808		0.047 / 1.839		6%↑	0%↑
NLOS_2	0.066 / 1.996		0.055 / 1.951		0.054 / 1.949		18%↑	2%↑
NLOS_3	0.058 / 2.013		0.056 / 2.034		0.053 / 1.986		9%↑	1%↑
NLOS_4	0.069 / 2.119		0.060 / 2.067		0.059 / 2.093		14%↑	1%↑
SDM_1	0.087 / 3.075		0.039 / 2.157		0.039 / 2.089		55%↑	32%↑
SDM_2	0.068 / 2.135		0.031 / 1.857		0.030 / 1.735		56%↑	19%↑
SDM_3	0.079 / 3.890		0.032 / 2.468		0.032 / 2.139		59%↑	45%↑
SDM_4	0.086 / 2.416		0.034 / 1.948		0.033 / 1.856		62%↑	23%↑
HDM_1	0.230 / 2.762		0.200 / 2.599		0.134 / 2.373		42%↑	14%↑
HDM_2	0.165 / 2.120		0.146 / 2.269		0.100 / 1.874		39%↑	12%↑
HDM_3	0.205 / 2.648		0.108 / 2.274		0.082 / 1.768		60%↑	33%↑
HDM_4	0.174 / 2.643		0.123 / 2.341		0.096 / 1.961		45%↑	26%↑

with DT, CT-Full_(H) reduces position error by 6% ~ 18% for smooth motion, 55% ~ 62% for shift-speed motion, and 39% ~ 60% for high-speed motion. The accuracy gains grow with motion dynamics and observation dropouts, as illustrated in Fig. 18. Notably, CT-BCD_(I) closely approaches CT-Full_(H) while consistently outperforming DT, showing that it achieves near-global consistency after sufficient iterations. Moreover, CT-RIO benefits substantially from complete-trajectory optimization, especially under shift-speed and high-speed motion, whereas DT shows little or even negative improvement (e.g., in **SDM**). This highlights that CT-RIO better exploits global consistency for offline estimation, while DT remains limited by its local formulation.

B. Online Time-Offset Estimation

This section evaluates the real-world performance of the proposed online time-offset estimation in the CT-RIO framework. The experiments are conducted on the **TUS** sequences, and the quantitative results are summarized in Tab. IX.

For each sequence, Devices 1 ~ 4 exhibit initial temporal offsets ranging from several tens to hundreds of milliseconds with respect to Device 0. Under these challenging conditions, DT suffers from severe performance degradation due to its inability to model or compensate for time-offsets. In contrast, the CT-Full already demonstrates improved robustness even without explicit time-offset estimation. CT-Full consistently outperforms the DT baseline. When online estimation of the time-offset τ is enabled, the performance improves substantially across all sequences. Taking TUS_1 as an example, the average position error is reduced from 0.139 m to 0.092 m, while the rotation error decreases from 11.8° to 1.9°. Similar trends are observed across TUS_2 to TUS_4. In addition, the estimated offsets closely match the measured ground truth. Across all sequences, the deviation remains within 1 ms, confirming both accuracy and consistency. Given that the sensors on the CREPES-X device provide timestamps with

TABLE IX: ABLATION STUDY IN TIME-OFFSET ESTIMATION (LATEST OUTPUT, COLOR DEFINITION: BEST, SECOND-BEST, DETERMINED BY POSITION RMSE, AND BY ROTATION RMSE IF EQUAL)

Exp.	Dev.	DT		CT-Full		CT-Full with τ Estimation	
		Pos (m)	Rot (°)	Pos (m)	Rot (°)	Pos (m)	Rot (°)
TUS_1	1	0.255 / 9.2		0.136 / 8.5		0.103 / 2.0	
	2	0.167 / 7.6		0.111 / 8.0		0.065 / 1.7	
	3	0.132 / 6.7		0.130 / 6.9		0.110 / 1.9	
	4	0.315 / 24.4		0.174 / 23.9		0.089 / 2.0	
TUS_2	1	0.227 / 9.8		0.130 / 9.4		0.083 / 1.6	
	2	0.203 / 11.7		0.127 / 10.1		0.063 / 1.5	
	3	0.125 / 7.7		0.120 / 7.7		0.097 / 1.7	
	4	0.294 / 18.9		0.133 / 18.0		0.068 / 1.9	
TUS_3	1	0.294 / 9.2		0.149 / 9.4		0.106 / 2.0	
	2	0.193 / 12.3		0.128 / 10.8		0.067 / 2.0	
	3	0.146 / 5.9		0.123 / 5.6		0.107 / 2.2	
	4	0.288 / 22.0		0.152 / 20.9		0.084 / 2.0	
TUS_4	1	0.247 / 11.7		0.145 / 9.9		0.106 / 2.9	
	2	0.206 / 14.5		0.150 / 13.6		0.071 / 2.0	
	3	0.134 / 5.7		0.129 / 5.7		0.111 / 2.9	
	4	0.223 / 19.1		0.135 / 18.6		0.080 / 3.0	

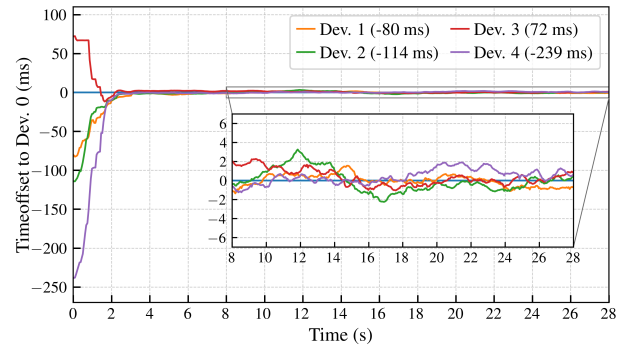


Fig. 20. Time-offset estimation error curves of all devices in TUS_1. The estimates converge rapidly from various initial offsets and remain stable throughout the sequence.

millisecond-level resolution, this level of accuracy effectively achieves reliable time synchronization in practice.

We further visualize the online time-offset estimation process of CT-RIO on the TUS_1 sequence in Fig. 19. As shown in Fig. 19(a), the initial misalignment (when $T = 0$ s) of the bearing observations gradually improves, aligning with the target position as the time-offset is corrected (when $T = 2$ s). This indicates that the estimated time-offsets converge within approximately 2 seconds. In contrast, DT lacks time-offset estimation, resulting in continuously misaligned bearing observations, as seen in Fig. 19(b). Consequently, the incorrect observation timestamps lead to significant errors in both position and attitude estimation. This effect is evident in Fig. 19(c) and Fig. 19(d), where DT shows large error spikes, while CT-RIO maintains accuracy similar to other hard-synchronized sequences. Finally, Fig. 20 illustrates the convergence behavior of the estimated time-offsets for all devices in TUS_1. The estimates rapidly converge from large initial offsets and remain stable throughout the sequence.

Overall, these results demonstrate that the proposed method not only achieves reliable time-offset estimation under real-world noise, but also directly improves the quality of trajectory estimation across diverse sequences.

TABLE X: POSITION RMSE AND OPTIMIZATION TIME OF NON-UNIFORM AND UNIFORM B-SPLINES WITH DIFFERENT KNOT FREQUENCY (COMPLETE TRAJECTORY, COLOR DEFINITION: BEST, SECOND-BEST, DETERMINED BY POSITION RMSE, AND BY OPTIMIZATION TIME IF EQUAL)

Exp.	Uni-50	Uni-20	Uni-10	Uni-5	Non-Uniform	
	Pos / Time (m) / (ms)	Freq. (Hz)				
LOS	0.061 / 120	0.061 / 115	0.062 / 107	0.066 / 99	0.060 / 105	12.8
NLOS	0.051 / 130	0.053 / 100	0.055 / 91	0.062 / 83	0.053 / 97	10.9
SDM	0.035 / 102	0.038 / 81	0.040 / 79	0.101 / 81	0.034 / 73	18.5
HDM	0.104 / 155	0.104 / 96	0.105 / 90	0.161 / 93	0.103 / 95	30.3

TABLE XI: RMSE OF NON-UNIFORM AND UNIFORM B-SPLINES WITH DIFFERENT KNOT FREQUENCY FOR DIFFERENT DEVICE IN SDM SERIES (COMPLETE TRAJECTORY, COLOR DEFINITION: BEST, SECOND-BEST, DETERMINED BY POSITION RMSE, AND BY ROTATION RMSE IF EQUAL)

Exp.	Dev.	Uni-50	Uni-20	Uni-10	Uni-5	Non-Uniform	
		Pos / Rot (m) / (°)	Freq. (Hz)				
SDM_1	1	0.039 / 2.1	0.042 / 2.2	0.047 / 3.3	0.182 / 25.7	0.039 / 2.1	19.2
	&	0.011 / 0.5	0.013 / 0.5	0.013 / 0.5	0.013 / 0.6	0.011 / 0.5	5.0
SDM_2	1	0.032 / 1.7	0.035 / 1.8	0.037 / 1.9	0.052 / 4.6	0.030 / 1.7	16.9
	&	0.011 / 0.6	0.011 / 0.6	0.010 / 0.6	0.010 / 0.6	0.008 / 0.5	5.0
SDM_3	1	0.035 / 2.5	0.037 / 2.2	0.038 / 2.7	0.121 / 20.8	0.032 / 2.1	17.9
	&	0.010 / 0.8	0.009 / 0.8	0.009 / 0.8	0.012 / 0.9	0.008 / 0.7	5.0
SDM_4	1	0.033 / 1.9	0.037 / 1.9	0.038 / 2.0	0.050 / 5.3	0.033 / 1.9	20.1
	&	0.013 / 0.4	0.013 / 0.4	0.013 / 0.4	0.013 / 0.4	0.009 / 0.4	5.0

& Denotes the average result of Devices 2 ~ 4.

C. Comparison of Non-Uniform and Uniform Knot Frequency

We evaluate the necessity of non-uniform knot insertion on the real-world sequences. Tab. X reports the RMSE and optimization time of B-splines under uniform knot spacing at frequency f Hz (*Uni- f*) and under the proposed relative-motion-intensity-aware non-uniform scheme (*Non-Uniform*).

As shown in Tab. X, with uniform knot frequency, increasing knot density improves trajectory accuracy at the expense of higher computation. The densest setting, *Uni-50*, yields the best accuracy in all cases, but *Uni-20* achieves comparable performance in **LOS** and **HDM** with much lower cost, showing that extreme density is often unnecessary. Overly sparse distributions struggle under fast motion: while *Uni-5* performs well in mild scenarios (**LOS**, **NLOS**, and stationary devices in **SDM**), it degrades significantly for high-speed motion, especially for moving Device 1 in **SDM** and **HDM**. In many cases, *Uni-10* maintains high computational efficiency without sacrificing too much accuracy, consistent with prior findings reported in [30].

For non-uniform knot frequency, the proposed *Non-Uniform* keyknot strategy (Sec. V-C) adaptively adjusts keyknot placement according to motion complexity. As a result, it achieves the best or second-best accuracy across all sequences, while notably improving efficiency compared with the densest uniform knot configuration, which also yields high accuracy. Specifically, it reduces computation time by 13% to 39%..

To further illustrate the effect of knot distribution, we analyze the results for Device 1 in the **SDM_1** sequence. Fig. 21(a) and (b) show that the *Non-Uniform* strategy concentrates knots in fast-motion regions while sparsifying them in slower segments, leading to efficient resource utilization. This adaptive allocation directly contributes to the error behavior observed in Fig. 21(c), where uniform methods exhibit large

error fluctuations during high-speed intervals. In contrast, *Non-Uniform* maintains consistently lower errors throughout the trajectory. Overall, *Non-Uniform* adapts to motion complexity, reduces errors, and improves computational efficiency compared with fixed-frequency baselines.

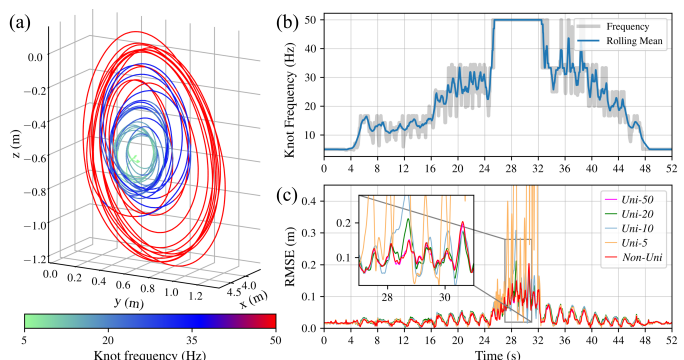


Fig. 21. The results of CT-Full in **SDM_1**. (a) Trajectory of Device 1, colored by knot frequency. (b) Knot frequency along the full trajectory of the non-uniform B-spline. (c) Position RMSE of non-uniform and uniform B-splines with different knot frequencies.

Beyond the accuracy improvement demonstrated in this experiment, another essential advantage of the proposed non-uniform scheme lies in its capability to support dense knot insertion. This property has already been validated in the benchmark evaluation in Sec. VI-D, where CT-BCD achieves reliable high-frequency performance.

VIII. CONCLUSION

In this paper, we presented CT-RIO, a continuous-time direct relative localization and time synchronization system for robot swarms. CT-RIO operates purely on relative kinematics, fusing asynchronous inter-robot observations and inertial data via a sliding-window formulation. By novelly leveraging clamped non-uniform B-splines, it eliminates the query-time delay of prior unclamped non-uniform methods and enables endpoint interpolation for real-time evaluation and initialization. Closed-form extension and shrinkage routines that modify only a minimal set of boundary control points preserve the shape of previously optimized segments, allowing the proposed *knot-keyknot* strategy to deliver high-frequency outputs while retaining only motion-informative keyknots. To ensure scalability, we decompose the full problem into agent-wise sub-problems solved via an IA-BCD algorithm, with periodic global refinement restoring consistency. Extensive simulations and real-world experiments demonstrate that CT-RIO effectively estimates both relative poses and time-offsets, consistently outperforming the state-of-the-art discrete-time baseline in both accuracy and frequency.

Despite these benefits, CT-RIO has limitations that open avenues for future work. First, extending clamped splines to broader estimation tasks (e.g., loop-closure SLAM) raises challenges such as maintaining loop-consistency, handling marginalization under spline edits, and preserving the information structure. Second, while this paper provides a convergence analysis for the proposed IA-BCD algorithm, the resulting conditions should be interpreted primarily as design guidance

rather than as tight practical guarantees. In particular, the derived lower bound on the damping parameter is sufficient but highly conservative, and thus does not directly offer a realistic guideline for parameter selection in real systems. Thus, developing more practically meaningful bounds remains an important direction for future work. Third, the keyknot selection criteria in this work are empirically chosen, and a more principled approach that considers the information gain of each knot would be beneficial. Finally, further investigation of fully distributed and certifiably convergent variants that scale to large swarms is warranted.

ACKNOWLEDGMENT

The authors would like to thank Chice Xuan, Zhihao Tian, and Tienan Zhang for their assistance in hardware implementation. The authors would like to thank Juncheng Chen, Nanhe Chen, Zhenyu Hou, Mingwei Lai, Tiancheng Lai, Xiangyu Li, Wentao Liu, Ruitian Pang, Pengfei Wang, Shuo Wang, Xingpeng Wang, Ge Wan, Wenkai Xiao, Miao Xu, Jiajun Yu, Mengke Zhang, and Mingxuan Zhang for their assistance in conducting real-world experiments.

REFERENCES

- [1] S. Waharte and N. Trigoni, "Supporting search and rescue operations with uavs," in *2010 international conference on emerging security technologies*. IEEE, 2010, pp. 142–147.
- [2] T. Sherman, J. Tellez, T. Cady, J. Herrera, H. Haideri, J. Lopez, M. Caudle, S. Bhandari, and D. Tang, "Cooperative search and rescue using autonomous unmanned aerial vehicles," in *2018 AIAA Information Systems-AIAA Infotech@ Aerospace*, 2018, p. 1490.
- [3] Y. Tian, K. Liu, K. Ok, L. Tran, D. Allen, N. Roy, and J. P. How, "Search and rescue under the forest canopy using multiple uavs," *The International Journal of Robotics Research*, vol. 39, no. 10-11, pp. 1201–1221, 2020.
- [4] Y. Gao, Y. Wang, X. Zhong, T. Yang, M. Wang, Z. Xu, Y. Wang, Y. Lin, C. Xu, and F. Gao, "Meeting-merging-mission: A multi-robot coordinate framework for large-scale communication-limited exploration," in *2022 IEEE/RSJ International Conference on Intelligent Robots and Systems (IROS)*. IEEE, 2022, pp. 13 700–13 707.
- [5] B. Zhou, H. Xu, and S. Shen, "Racer: Rapid collaborative exploration with a decentralized multi-uav system," *IEEE Transactions on Robotics*, vol. 39, no. 3, pp. 1816–1835, 2023.
- [6] L. Montesano, J. Gaspar, J. Santos-Victor, and L. Montano, "Cooperative localization by fusing vision-based bearing measurements and motion," in *2005 IEEE/RSJ International Conference on Intelligent Robots and Systems*. IEEE, 2005, pp. 2333–2338.
- [7] X. S. Zhou and S. I. Roumeliotis, "Robot-to-robot relative pose estimation from range measurements," *IEEE Transactions on Robotics*, vol. 24, no. 6, pp. 1379–1393, 2008.
- [8] P. Stegagno, M. Cognetti, L. Rosa, P. Peliti, and G. Oriolo, "Relative localization and identification in a heterogeneous multi-robot system," in *2013 IEEE international conference on robotics and automation*. IEEE, 2013, pp. 1857–1864.
- [9] B. Jiang, B. D. Anderson, and H. Hmam, "3-d relative localization of mobile systems using distance-only measurements via semidefinite optimization," *IEEE Transactions on Aerospace and Electronic Systems*, vol. 56, no. 3, pp. 1903–1916, 2019.
- [10] M. Li, G. Liang, H. Luo, H. Qian, and T. L. Lam, "Robot-to-robot relative pose estimation based on semidefinite relaxation optimization," in *2020 IEEE/RSJ International Conference on Intelligent Robots and Systems (IROS)*. IEEE, 2020, pp. 4491–4498.
- [11] S. Chen, Y. Li, and W. Dong, "High-performance relative localization based on key-node seeking considering aerial drags using range and odometry measurements," *IEEE Transactions on Industrial Electronics*, vol. 71, no. 6, pp. 6021–6031, 2023.
- [12] Y. Wang, X. Wen, Y. Cao, C. Xu, and F. Gao, "Bearing-based relative localization for robotic swarm with partially mutual observations," *IEEE Robotics and Automation Letters*, vol. 8, no. 4, pp. 2142–2149, 2023.
- [13] L. Chen, C. Liang, S. Yuan, M. Cao, and L. Xie, "Relative localizability and localization for multi-robot systems," *IEEE Transactions on Robotics*, 2025.
- [14] E. Olson, "Apriltag: A robust and flexible visual fiducial system," in *2011 IEEE international conference on robotics and automation*. IEEE, 2011, pp. 3400–3407.
- [15] M. Faessler, E. Mueggler, K. Schwabe, and D. Scaramuzza, "A monocular pose estimation system based on infrared leds," in *2014 IEEE international conference on robotics and automation (ICRA)*. IEEE, 2014, pp. 907–913.
- [16] D. Dias, R. Ventura, P. Lima, and A. Martinoli, "On-board vision-based 3d relative localization system for multiple quadrotors," in *2016 IEEE International Conference on Robotics and Automation (ICRA)*. IEEE, 2016, pp. 1181–1187.
- [17] V. Walter, M. Saska, and A. Franchi, "Fast mutual relative localization of uavs using ultraviolet led markers," in *2018 International Conference on Unmanned Aircraft Systems (ICUAS)*. IEEE, 2018, pp. 1217–1226.
- [18] A. Fishberg and J. P. How, "Multi-agent relative pose estimation with uwb and constrained communications," in *2022 IEEE/RSJ International Conference on Intelligent Robots and Systems (IROS)*. IEEE, 2022, pp. 778–785.
- [19] A. Fishberg, B. Quiter, and J. P. How, "Murp: Multi-agent ultra-wideband relative pose estimation with constrained communications in 3d environments," *IEEE Robotics and Automation Letters*, 2024.
- [20] C. C. Cossette, M. A. Shalaby, D. Saussié, J. Le Ny, and J. R. Forbes, "Optimal multi-robot formations for relative pose estimation using range measurements," in *2022 IEEE/RSJ International Conference on Intelligent Robots and Systems (IROS)*. IEEE, 2022, pp. 2431–2437.
- [21] F. Aghili and C.-Y. Su, "Robust relative navigation by integration of icp and adaptive kalman filter using laser scanner and imu," *IEEE/ASME Transactions on Mechatronics*, vol. 21, no. 4, pp. 2015–2026, 2016.
- [22] Z. Xun, J. Huang, Z. Li, Z. Ying, Y. Wang, C. Xu, F. Gao, and Y. Cao, "Crepes: Cooperative relative pose estimation system," in *2023 IEEE/RSJ International Conference on Intelligent Robots and Systems (IROS)*. IEEE, 2023, pp. 5274–5281.
- [23] R. Armani and C. Holz, "Accurately tracking relative positions of moving trackers based on uwb ranging and inertial sensing without anchors," in *2024 IEEE/RSJ International Conference on Intelligent Robots and Systems (IROS)*. IEEE, 2024, pp. 12 515–12 521.
- [24] H. Zhao, L. Xu, Y. Li, F. Wen, H. Gao, C. Liu, J. Yu, Y. Wang, and Y. Shen, "Robust and scalable multi-robot localization using stereo uwb arrays," *IEEE Transactions on Robotics*, 2025.
- [25] Z. Li, Z. Wang, J. Lu, Q. Liu, Z. Xun, Y. Wang, F. Gao, C. Xu, and Y. Cao, "Crepes-x: Hierarchical bearing-distance-inertial direct cooperative relative pose estimation system," *arXiv preprint arXiv:2512.24688*, 2025.
- [26] M. A. Shalaby, C. C. Cossette, J. Le Ny, and J. R. Forbes, "Multi-robot relative pose estimation and imu preintegration using passive uwb transceivers," *IEEE transactions on robotics*, 2024.
- [27] P. Chen and Z. Yang, "Understanding ptp performance in today's wi-fi networks," *IEEE/ACM Transactions on Networking*, vol. 31, no. 6, pp. 3037–3050, 2023.
- [28] X. Wen, Y. Wang, X. Zheng, K. Wang, C. Xu, and F. Gao, "Simultaneous time synchronization and mutual localization for multi-robot system," in *2024 IEEE International Conference on Robotics and Automation (ICRA)*. IEEE, 2024, pp. 2603–2609.
- [29] J. Lv, X. Lang, J. Xu, M. Wang, Y. Liu, and X. Zuo, "Continuous-time fixed-lag smoothing for lidar-inertial-camera slam," *IEEE/ASME Transactions on Mechatronics*, 2023.
- [30] G. Cioffi, T. Cieslewski, and D. Scaramuzza, "Continuous-time vs. discrete-time vision-based slam: A comparative study," *IEEE Robotics and Automation Letters*, vol. 7, no. 2, pp. 2399–2406, 2022.
- [31] J. Rehder, J. Nikolic, T. Schneider, T. Hinzmann, and R. Siegwart, "Extending kalibr: Calibrating the extrinsics of multiple imus and of individual axes," in *2016 IEEE International Conference on Robotics and Automation (ICRA)*. IEEE, 2016, pp. 4304–4311.
- [32] C. Sommer, V. Usenko, D. Schubert, N. Demmel, and D. Cremers, "Efficient derivative computation for cumulative b-splines on lie groups," in *Proceedings of the IEEE/CVF Conference on Computer Vision and Pattern Recognition*, 2020, pp. 11 148–11 156.
- [33] J. Lv, X. Zuo, K. Hu, J. Xu, G. Huang, and Y. Liu, "Observability-aware intrinsic and extrinsic calibration of lidar-imu systems," *IEEE Transactions on Robotics*, vol. 38, no. 6, pp. 3734–3753, 2022.
- [34] S. Chen, X. Li, S. Li, Y. Zhou, and X. Yang, "ikalibr: Unified targetless spatiotemporal calibration for resilient integrated inertial systems," *IEEE Transactions on Robotics*, 2025.

- [35] E. Mueggler, G. Gallego, H. Rebecq, and D. Scaramuzza, "Continuous-time visual-inertial odometry for event cameras," *IEEE Transactions on Robotics*, vol. 34, no. 6, pp. 1425–1440, 2018.
- [36] V. Usenko, N. Demmel, D. Schubert, J. Stückler, and D. Cremers, "Visual-inertial mapping with non-linear factor recovery," *IEEE Robotics and Automation Letters*, vol. 5, no. 2, pp. 422–429, 2019.
- [37] C. Park, P. Moghadam, J. L. Williams, S. Kim, S. Sridharan, and C. Fookes, "Elasticity meets continuous-time: Map-centric dense 3d lidar slam," *IEEE Transactions on Robotics*, vol. 38, no. 2, pp. 978–997, 2021.
- [38] J. Lv, K. Hu, J. Xu, Y. Liu, X. Ma, and X. Zuo, "Clins: Continuous-time trajectory estimation for lidar-inertial system," in *2021 IEEE/RSJ International Conference on Intelligent Robots and Systems (IROS)*. IEEE, 2021, pp. 6657–6663.
- [39] X. Lang, J. Lv, J. Huang, Y. Ma, Y. Liu, and X. Zuo, "Ctrl-vio: Continuous-time visual-inertial odometry for rolling shutter cameras," *IEEE Robotics and Automation Letters*, vol. 7, no. 4, pp. 11 537–11 544, 2022.
- [40] X. Lang, C. Chen, K. Tang, Y. Ma, J. Lv, Y. Liu, and X. Zuo, "Coco-lic: continuous-time tightly-coupled lidar-inertial-camera odometry using non-uniform b-spline," *IEEE Robotics and Automation Letters*, 2023.
- [41] D. Hug, I. Alzugaray, and M. Chli, "Hyperion—a fast, versatile symbolic gaussian belief propagation framework for continuous-time slam," in *European Conference on Computer Vision*. Springer, 2024, pp. 215–231.
- [42] X. Lang, J. Lv, K. Tang, L. Li, J. Huang, L. Liu, Y. Liu, and X. Zuo, "Gaussian-lic2: Lidar-inertial-camera gaussian splatting slam," *arXiv preprint arXiv:2507.04004*, 2025.
- [43] P. Stegagno, M. Cagnetti, G. Oriolo, H. H. Bühlhoff, and A. Franchi, "Ground and aerial mutual localization using anonymous relative-bearing measurements," *IEEE Transactions on Robotics*, vol. 32, no. 5, pp. 1133–1151, 2016.
- [44] J. Huai, Y. Lin, Y. Zhuang, C. K. Toth, and D. Chen, "Observability analysis and keyframe-based filtering for visual inertial odometry with full self-calibration," *IEEE Transactions on Robotics*, vol. 38, no. 5, pp. 3219–3237, 2022.
- [45] T. Qin and S. Shen, "Online temporal calibration for monocular visual-inertial systems," in *2018 IEEE/RSJ International Conference on Intelligent Robots and Systems (IROS)*. IEEE, 2018, pp. 3662–3669.
- [46] P. Furgale, J. Rehder, and R. Siegwart, "Unified temporal and spatial calibration for multi-sensor systems," in *2013 IEEE/RSJ International Conference on Intelligent Robots and Systems*. IEEE, 2013, pp. 1280–1286.
- [47] J. Sun, W. Sun, G. Zhang, K. Yang, S. Li, X. Meng, N. Deng, and C. Tan, "Ct-uo: Continuous-time uwb-inertial-odometer localization using non-uniform b-spline with fewer anchors," *arXiv preprint arXiv:2502.06287*, 2025.
- [48] A. Cunningham, V. Indelman, and F. Dellaert, "Ddf-sam 2.0: Consistent distributed smoothing and mapping," in *2013 IEEE international conference on robotics and automation*. IEEE, 2013, pp. 5220–5227.
- [49] H. Xu, P. Liu, X. Chen, and S. Shen, "D² slam: Decentralized and distributed collaborative visual-inertial slam system for aerial swarm," *IEEE Transactions on Robotics*, vol. 40, pp. 3445–3464, 2024.
- [50] R. Murai, J. Ortiz, S. Saeedi, P. H. Kelly, and A. J. Davison, "A robot web for distributed many-device localization," *IEEE Transactions on Robotics*, vol. 40, pp. 121–138, 2023.
- [51] R. Murai, I. Alzugaray, P. H. Kelly, and A. J. Davison, "Distributed simultaneous localisation and auto-calibration using gaussian belief propagation," *IEEE Robotics and Automation Letters*, vol. 9, no. 3, pp. 2136–2143, 2024.
- [52] Y. Tian, A. Koppel, A. S. Bedi, and J. P. How, "Asynchronous and parallel distributed pose graph optimization," *IEEE Robotics and Automation Letters*, vol. 5, no. 4, pp. 5819–5826, 2020.
- [53] A. Thoms, A. Papalia, J. Velasquez, D. M. Rosen, and S. Narasimhan, "Distributed certifiably correct range-aided slam," *arXiv preprint arXiv:2503.03192*, 2025.
- [54] Y. Liu, Y. Wang, J. Wang, and Y. Shen, "Distributed 3d relative localization of uavs," *IEEE Transactions on Vehicular Technology*, vol. 69, no. 10, pp. 11 756–11 770, 2020.
- [55] T. Wu, G. Zaitian, Q. Wang, and F. Gao, "Scalable distance-based multi-agent relative state estimation via block multiconvex optimization," *arXiv preprint arXiv:2405.20883*, 2024.
- [56] T. Sun, R. Hannah, and W. Yin, "Asynchronous coordinate descent under more realistic assumptions," *Advances in Neural Information Processing Systems*, vol. 30, 2017.
- [57] K. Qin, "General matrix representations for b-splines," in *Proceedings Pacific Graphics '98. Sixth Pacific Conference on Computer Graphics and Applications (Cat. No. 98EX208)*. IEEE, 1998, pp. 37–43.
- [58] M.-J. Kim, M.-S. Kim, and S. Y. Shin, "A general construction scheme for unit quaternion curves with simple high order derivatives," in *Proceedings of the 22nd annual conference on Computer graphics and interactive techniques*, 1995, pp. 369–376.
- [59] L. Piegl and W. Tiller, *The NURBS book*. Springer Science & Business Media, 2012.
- [60] D. L. Christensen, L. Shumway, R. W. Beard, and T. W. McLain, "Non-uniform b-spline trajectory optimization using control point representation transformations," in *2025 American Control Conference (ACC)*. IEEE, 2025, pp. 515–522.
- [61] S.-M. Hu, C.-L. Tai, and S.-H. Zhang, "An extension algorithm for b-splines by curve unclamping," *Computer-Aided Design*, vol. 34, no. 5, pp. 415–419, 2002.
- [62] T. Qin, P. Li, and S. Shen, "Vins-mono: A robust and versatile monocular visual-inertial state estimator," *IEEE Transactions on Robotics*, vol. 34, no. 4, pp. 1004–1020, 2018.
- [63] B. Zhang, X. Chen, Z. Li, G. Beltrame, C. Xu, F. Gao, and Y. Cao, "Coni-mpc: Cooperative non-inertial frame based model predictive control," *IEEE Robotics and Automation Letters*, 2023.
- [64] S. Agarwal, K. Mierle, and T. C. S. Team, "Ceres Solver," 10 2023. [Online]. Available: <https://github.com/ceres-solver/ceres-solver>
- [65] S. K. Mani, R. Durairajan, P. Barford, and J. Sommers, "Mntp: Enhancing time synchronization for mobile devices," in *Proceedings of the 2016 Internet Measurement Conference*, 2016, pp. 335–348.
- [66] A. Yershova, S. Jain, S. M. LaValle, and J. C. Mitchell, "Generating uniform incremental grids on so (3) using the hopf fibration," *The International Journal of Robotics Research*, vol. 29, no. 7, pp. 801–812, 2010.
- [67] Z. Zhang and D. Scaramuzza, "A tutorial on quantitative trajectory evaluation for visual (-inertial) odometry," in *2018 IEEE/RSJ International Conference on Intelligent Robots and Systems (IROS)*. IEEE, 2018, pp. 7244–7251.
- [68] H. Robbins and D. Siegmund, "A convergence theorem for non negative almost supermartingales and some applications," in *Optimizing methods in statistics*. Elsevier, 1971, pp. 233–257.

APPENDIX A
B-SPLINES

In the following, we first provide the formal definition of B-splines and the corresponding basis matrix formulation, and analyze the valid query interval of B-spline trajectories.

Knots	t_0	t_1	t_2	t_3	t_4	t_5	t_6	t_7	t_8	t_9
Basis Functions	$B_{0,1}$	$B_{1,1}$	$B_{2,1}$	$B_{3,1}$	$B_{4,1}$	$B_{5,1}$	$B_{6,1}$	$B_{7,1}$	$B_{8,1}$	
	$B_{0,2}$	$B_{1,2}$	$B_{2,2}$	$B_{3,2}$	$B_{4,2}$	$B_{5,2}$	$B_{6,2}$	$B_{7,2}$		
	$B_{0,3}$	$B_{1,3}$	$B_{2,3}$	$B_{3,3}$	$B_{4,3}$	$B_{5,3}$	$B_{6,3}$			
	$B_{0,4}$	$B_{1,4}$	$B_{2,4}$	$B_{3,4}$	$B_{4,4}$	$B_{5,4}$	$B_{6,4}$	$B_{7,4}$	$B_{8,4}$	$B_{9,4}$

Non-Zero

Fig. 22. A cubic B-spline with the newest knot at t_8 (blue part is undefined). The latest valid query interval is $[t_5, t_6)$. Although $B_{5,4}$ depends on $B_{6,3}$ which is undefined due to unknown t_9 , (28) shows that $B_{6,3} = 0$ for $t \in [t_5, t_6)$, so $B_{5,4}$ is fully defined within this interval.

A. Standard Definition of B-Splines

The translation B-spline curve of order k (degree $k-1$) is defined by a knot vector $\mathbf{T} = \{t_{[0]}, t_{[1]}, \dots, t_{[n+k]}\}$, control points $\mathbf{x}_p = \{\mathbf{p}_0, \mathbf{p}_1, \dots, \mathbf{p}_n\}$ and a set of basis functions $\mathbf{B} = \{B_{0,k}(t), B_{1,k}(t), \dots, B_{n,k}(t)\}$:

$$\mathbf{p}(t) = \sum_{i=0}^n B_{i,k}(t) \mathbf{p}_i, \quad (27)$$

where i is the index of the basis function and k is the order of the B-spline, the basis functions are given by the *Cox-de Boor* recursion formula:

$$B_{i,1}(t) = \begin{cases} 1, & t \in [t_{[i]}, t_{[i+1]}) \\ 0, & \text{otherwise} \end{cases}$$

$$B_{i,j}(t) = \begin{cases} u_0 B_{i,j-1}(t) + u_1 B_{i+1,j-1}(t), & t \in [t_{[i]}, t_{[i+j]}) \\ 0, & \text{otherwise} \end{cases}$$

$$u_0 = \frac{t - t_{[i]}}{t_{[i+j]} - t_{[i]}}, \quad u_1 = \frac{t_{[i+j+1]} - t}{t_{[i+j+1]} - t_{[i+1]}}. \quad (28)$$

Remark 1. For a B-spline of order k and $t \in [t_{[i]}, t_{[i+1]})$, only k basis functions $\{B_{i-k+1,k}(t), \dots, B_{i,k}(t)\}$ are non-zero, which depends on $2k$ knots $\{t_{[i-k+1]}, \dots, t_{[i+k]}\}$.

B. Matrix Representation of B-splines

The matrix form of B-splines enables efficient evaluation and supports the above analysis. As shown in [57], we can represent the B-spline curve in a matrix form. The value of $\mathbf{p}(t)$ at time $t \in [t_i, t_{i+1})$ can be expressed as:

$$\mathbf{p}(t) = \underbrace{[\mathbf{p}_{i-k+1}, \mathbf{p}_{i-k+2}, \dots, \mathbf{p}_i]}_{3 \times k} \underbrace{\mathbf{M}_i^{(k)}}_{k \times k} \mathbf{u}, \quad (29)$$

$$\mathbf{u} = [1, u, \dots, u^{k-1}], \quad u = (t - t_{[i]}) / (t_{[i+1]} - t_{[i]}),$$

where $\mathbf{M}_i^{(k)}$ is the i th blend matrix of the basis functions:

$$\begin{cases} \mathbf{M}_i^{(j)} = \begin{bmatrix} \mathbf{M}_i^{(j-1)} \\ \mathbf{0} \end{bmatrix} \mathbf{N}_0^{(j)} + \begin{bmatrix} \mathbf{0} \\ \mathbf{M}_i^{(j-1)} \end{bmatrix} \mathbf{N}_1^{(j)} \\ \mathbf{M}_i^{(1)} = [1] \end{cases} \quad (30)$$

where

$$\mathbf{N}_0^{(j)} = \begin{bmatrix} 1 - \delta_{0,i-j+2} & \delta_{0,i-j+2} & & & \mathbf{0} \\ & 1 - \delta_{0,i-j+3} & \delta_{0,i-j+3} & & \\ & & \ddots & \ddots & \\ \mathbf{0} & & & 1 - \delta_{0,i} & \delta_{0,i} \\ & & & & \ddots & \ddots \end{bmatrix}$$

$$\mathbf{N}_1^{(j)} = \begin{bmatrix} -\delta_{1,i-j+2} & \delta_{1,i-j+2} & & & \mathbf{0} \\ & -\delta_{1,i-j+3} & \delta_{1,i-j+3} & & \\ & & \ddots & \ddots & \\ \mathbf{0} & & & -\delta_{1,i} & \delta_{1,i} \end{bmatrix} \quad (31)$$

and

$$\delta_{0,m} = \frac{t_{[i]} - t_{[m]}}{t_{[m+j-1]} - t_{[m]}}, \quad \delta_{1,m} = \frac{t_{[i+1]} - t_{[i]}}{t_{[m+j-1]} - t_{[m]}} \quad (32)$$

with the convention $0/0 = 0$.

It is also possible to use matrix representation for the cumulative splines:

$$\underbrace{\mathbf{p}(t)}_{3 \times 1} = \underbrace{[\mathbf{p}_{i-k+1}, \mathbf{d}_1^{i-k+1}, \dots, \mathbf{d}_{k-1}^{i-k+1}]}_{3 \times k} \underbrace{\widetilde{\mathbf{M}}_i^{(k)}}_{k \times k} \underbrace{\mathbf{u}}_{k \times 1}, \quad (33)$$

with cumulative matrix entries $\widetilde{m}_{j,n}^{(k)} = \sum_{s=j}^{k-1} m_{s,n}^{(k)}$ and difference vectors $\mathbf{d}_j^i = \mathbf{p}_{i+j} - \mathbf{p}_{i+j-1}$. Using the property of block matrix multiplication, (33) can be expanded as:

$$\mathbf{p}(t) = \mathbf{p}_{i-k+1} + \sum_{j=1}^{k-1} \lambda_j \cdot \mathbf{d}_j^{i-k+1} \quad (34)$$

where λ_j is the j -th element of the vector $\widetilde{\mathbf{M}}_i^{(k)} \mathbf{u}$.

The cumulative B-spline in (34) can be generalized to $SO(3)$ for smooth rotation generation. We can represent the rotation B-spline of order k over time $t \in [t_i, t_{i+1})$ as:

$$\mathbf{R}(t) = \mathbf{R}_{i-k+1} \cdot \prod_{j=1}^{k-1} \text{Exp}(\lambda_j \cdot \mathbf{d}_j^{i-k+1}), \quad (35)$$

where $\mathbf{d}_j^i = \text{Log}(\mathbf{R}_{i+j-1}^{-1} \mathbf{R}_{i+j})$, and $\mathbf{R}_i \in SO(3)$ is the i -th rotation control point. $\text{Exp}(\cdot)$ and $\text{Log}(\cdot)$ are the exponential and logarithmic maps of $SO(3)$.

Remark 2. A blend matrix and a spline queryable time interval always correspond to each other.

Remark 3. The blend matrix $\mathbf{M}_i^{(k)}$ only depends on $2k-2$ knots $\{t_{[i-k+2]}, \dots, t_{[i+k-1]}\}$.

C. Extended Query Interval Property of B-Splines

Remark 1 and Remark 3 seem contradictory on needed knots for query at $[t_{[i]}, t_{[i+1]})$, but they are essentially the same. For a B-spline of order k and $t \in [t_{[i]}, t_{[i+1]})$, the query only depends on $2k-2$ knots $\{t_{[i-k+2]}, \dots, t_{[i+k-1]}\}$ rather than $2k$ knots $\{t_{[i-k+1]}, \dots, t_{[i+k]}\}$, in spite of the basis function $B_{i-k+1,k}(t)$ depends on $t_{[i-k+1]}$ and $B_{i,k}(t)$ depends on $t_{[i+k]}$.

Take the right end $B_{i,k}(t)$ as example, it is computed by two lower-order basis functions $B_{i,k-1}(t)$ and $B_{i+1,k-1}(t)$. Note that $B_{i+1,k-1}(t)$ is zero in the interval $[t_{[i]}, t_{[i+1]})$. So $B_{i,k}(t)$ is fully defined in the interval $[t_{[i]}, t_{[i+1]})$. Therefore, query the B-spline in the interval $[t_{[i]}, t_{[i+1]})$ do not depend on

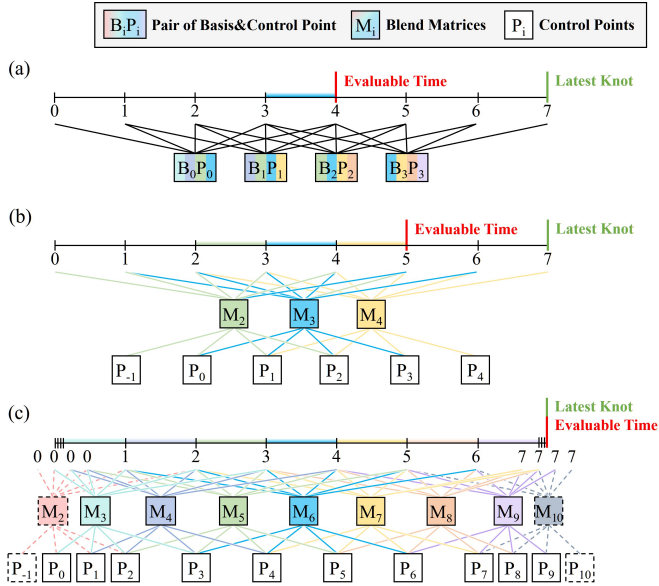


Fig. 23. (a) Recursive definition of B-splines shows that the spline can only be queried up to $t_{[n]}$ when the newest knot is $t_{[n+k-1]}$. (b) Matrix representation of B-splines clearly shows that one additional spline valid interval can be constructed on each side of the spline. (c) The additionally constructed control points \mathbf{p}_{-1} and \mathbf{p}_{n+1} are meaningless for clamped B-splines due to it not affecting the shape of the spline.

$t_{[i-k+1]}$ and $t_{[i+k]}$. See Fig. 22 for an example. This reveals the consistency between the B-spline definition and the matrix representation, where the query only requires $2k - 2$ knots.

Remark 4 (Extended Query Interval Property). *Since the required knot is reduced by one at both the beginning and end, the valid queryable range for a B-spline with defined knots is extended by a segment. For a B-spline of order k with knot vector $\mathbf{T} = \{t_{[0]}, t_{[1]}, \dots, t_{[n+k]}\}$, the valid query interval is $[t_{[k-2]}, t_{[n+2]}]$.*

When using the matrix representation of B-splines, it is appear that we can construct one additional control point on each side of the spline, as shown in Fig. 23. Thus for a B-spline of order k with knot vector $\mathbf{T} = \{t_{[0]}, t_{[1]}, \dots, t_{[n+k]}\}$, the control points can be defined as $\mathbf{x}_{\mathbf{p}} = \{\mathbf{p}_{-1}, \mathbf{p}_0, \dots, \mathbf{p}_{n+1}\}$. In this case, the matrix representation of the B-spline becomes:

$$\underbrace{\mathbf{p}(t)}_{3 \times 1} = \underbrace{[\mathbf{p}_{i-k+2}, \mathbf{p}_{i-k+3}, \dots, \mathbf{p}_{i+1}]}_{3 \times k} \underbrace{\mathbf{M}_i^{(k)}}_{k \times k} \underbrace{\mathbf{u}}_{k \times 1}, \quad (36)$$

The spline valid interval thus extends to $[t_{[k-2]}, t_{[n+2]}]$. Non-uniform unclamped B-spline based state estimation methods [40], [42], [47] employ this approach to eliminate the query delay as much as possible but last $k - 2$ segments still cannot be queried, as shown in Fig. 23.

D. Clamped B-splines

Based on the multiplicity of knots at the endpoints, B-splines can be classified into unclamped and clamped B-splines. Clamped B-splines repeat the first and last knots k times, ensuring that the curve interpolates the endpoints [59]:

$$\begin{aligned} \mathbf{T}_{\text{clamp}} &: t_{[0]} = \dots = t_{[k-1]} \leq \dots \leq t_{[n+1]} = \dots = t_{[n+k]}, \\ \mathbf{T}_{\text{unclamp}} &: t_{[0]} \leq t_{[1]} \leq \dots \leq t_{[n+k-1]} \leq t_{[n+k]}. \end{aligned} \quad (37)$$

This construction improves boundary behavior and is widely used in geometric modeling. In real-time state estimation, clamping also helps avoid evaluation delay at the curve's end.

Remark 5. *For clamped B-splines, the additionally constructed control points are no longer needed and meaningless. Take the right end as example, the additionally constructed control point \mathbf{p}_{n+1} related to the basis function $B_{n+1,k}(t)$ whose influence range is $[t_{[n+1]}, t_{[n+k]}]$, indicating that the additionally constructed control points do not affect the shape of the clamped spline curve. Therefore, the control points are remained as $\mathbf{x}_{\mathbf{p}} = \{\mathbf{p}_0, \mathbf{p}_1, \dots, \mathbf{p}_n\}$. The spline valid interval is $[t_{[0]}, t_{[n+k]}]$.*

Proposition 3. *For a spline of order k with knot vector $T = \{t_0, \dots, t_{n+k}\}$, modifying knots outside the interval $[t_{k-1}, t_{n+1}]$ (including changes in endpoint multiplicities) does not alter the spline space on that interval. Consequently, the fitting capability on this interval remains unchanged.*

Proof. The spline space is fully determined by: (i) the knot partition inside the interval, (ii) the polynomial degree $k - 1$ on each knot span, (iii) the continuity at interior knots determined by their multiplicities. Changes to knots outside $[t_{k-1}, t_{n+1}]$ do not affect the partition, the segment degrees, or the interior continuity structure within this interval. Hence the spline space on $[t_{k-1}, t_{n+1}]$ remains unchanged. \square

E. Time Derivatives of B-splines

B-splines provides closed-form analytic derivatives, enabling efficient Jacobian computations, handling of inertial measurements, and online time-offset estimation. The r -th order time derivative of the B-spline at time t

As mentioned before, B-splines provides closed-form analytical derivatives. The time derivatives of the translation B-spline expressed through (29) are given by:

$$\frac{d^n}{dt^n} \mathbf{p}(t) = [\mathbf{p}_{i-k+1}, \mathbf{p}_{i-k+2}, \dots, \mathbf{p}_i] \mathbf{M}^{(k)} \frac{d^n}{dt^n} \mathbf{u} \quad (38)$$

where the first-order and second-order derivatives correspond to velocity and acceleration in the global frame, respectively.

The time derivatives of the rotation b-spline are given by the Sommer et al.'s optimized recursive formula [32]:

$$\begin{aligned} \ddot{\mathbf{R}} &= \mathbf{R} \left(\left(\boldsymbol{\omega}^{(k)} \right)_{\wedge}^2 + \dot{\boldsymbol{\omega}}_{\wedge}^{(k)} \right), \\ \dot{\mathbf{R}} &= \mathbf{R} \boldsymbol{\omega}_{\wedge}^{(k)}. \end{aligned} \quad (39)$$

where angular velocity $\boldsymbol{\omega}^{(k)}$ and acceleration $\dot{\boldsymbol{\omega}}^{(k)}$ in the **local frame** are given by:

$$\begin{aligned} \dot{\boldsymbol{\omega}}^{(j)} &= \dot{\lambda}_{j-1} \boldsymbol{\omega}^{(j)} \times \mathbf{d}_{j-1} + A_{j-1}^{\top} \dot{\boldsymbol{\omega}}^{(j-1)} + \ddot{\lambda}_{j-1} \mathbf{d}_{j-1}, \\ \boldsymbol{\omega}^{(j)} &= \mathbf{A} \mathbf{d}_{A_{j-1}^{-1}} \boldsymbol{\omega}^{(j-1)} + \dot{\lambda}_{j-1} \mathbf{d}_{j-1} \in \mathbb{R}^d, \\ \boldsymbol{\omega}^{(1)} &= \mathbf{0} \in \mathbb{R}^d. \end{aligned} \quad (40)$$

with $\lambda_j = \widetilde{\mathbf{M}}^{(k)} \mathbf{u}$, $A_j = \text{Exp}(\lambda_j \mathbf{d}_j)$, $\mathbf{Ad}(\cdot)$ is adjoint map, and i was omitted for simplify notation.

F. Jacobians of B-splines

Furthermore, the Jacobians of the trajectory values with respect to the control points are also derivated in [32] (take rotation B-spline as an example):

$$\frac{df}{dR_{i+j}} = \frac{\partial f}{\partial \mathbf{d}_j} \cdot \frac{\partial \mathbf{d}_j}{\partial R_{i+j}} + \frac{\partial f}{\partial \mathbf{d}_{j+1}} \cdot \frac{\partial \mathbf{d}_{j+1}}{\partial R_{i+j}}. \quad (41)$$

for $j > 0$. For $j = 0$ we obtain

$$\frac{df}{dR_i} = \frac{\partial f}{\partial R_i} + \frac{\partial f}{\partial \mathbf{d}_1} \cdot \frac{\partial \mathbf{d}_1}{\partial R_i}. \quad (42)$$

where \mathbf{f} represents the queried value of the B-spline at time t , which may correspond to $R(t)$, $\omega(t)$, or $\dot{\omega}(t)$. Then we can compute the Jacobians of the needed residuals with respect to the control points by applying the chain rule, as long as the residual is formed by queried values \mathbf{f} .

APPENDIX B

CONVERGENCE ANALYSIS FOR ASYNCHRONOUS BCD

Our analysis adapts the asynchronous block-coordinate descent (A-BCD) framework of [56] to the Levenberg-Marquardt setting. While [56] considers gradient-descent updates, our LM-based update introduces both curvature regularization and Jacobian-dependent terms. These differences lead to nontrivial modifications in the descent inequality, the Lyapunov construction, and the conditions on the damping parameter λ . We therefore re-establish each step of the argument under LM dynamics.

A. Problem Formulation

We consider the A-BCD framework for solving nonlinear least squares problems of the form

$$\arg \min_x f(x) = f(x_1, \dots, x_N) = \frac{1}{2} \sum_{j=1}^M \|r_j\|^2, \quad (43)$$

where the global variable x is composed of several local parameter blocks updated asynchronously with bounded delays. We define the residual vector $r : \mathbb{R}^N \rightarrow \mathbb{R}^M$, $M \gg N$ as

$$r(x) = (r_1(x), r_2(x), \dots, r_M(x))^\top \quad (44)$$

In A-BCD, each thread independently updates the solution vector, one block at a time, leaving all other blocks unchanged. Each block update is a read-compute-update cycle. It begins with a thread reading x from shared memory and saving it in a local variable \hat{x} . The thread then computes an update for a selected block x_i based on the local copy \hat{x} , and finally writes the updated block back to shared memory. Because the block updates are asynchronous, when a block update is completed, the \hat{x} that is read and then used to compute this update can be outdated at the completion time. We define the delay ϵ as the maximum number of block updates that can occur between the time a thread reads x and the time it writes back the updated block. Specifically, the update using the Levenberg-Marquardt rule is modeled as

$$x_i^{k+1} = x_i^k + \Delta_i^k, \quad \Delta_i^k = -(J_i^\top J_i + \lambda I)^{-1} J_i^\top r(\hat{x}^k), \quad (45)$$

where \hat{x}^k is the local copy read at the start of the k -th update, and J_i is the Jacobian of the residuals with respect to block x_i evaluated at \hat{x}^k and λ is a damping parameter. We denote $H^k = (J^{k\top} J^k + \lambda I)$ and $g^k = J^{k\top} r(\hat{x}^k)$ for brevity.

B. Preliminaries

Our analysis uses the following standard inequalities. For any $x^1, x^2, \dots, x^K \in \mathbb{R}^N$ and $\epsilon > 0$, it holds that

$$\langle x^1, x^2 \rangle \leq \epsilon \|x^1\|^2 + \frac{1}{\epsilon} \|x^2\|^2, \quad (46)$$

$$\langle x^1, x^2 \rangle \leq \|x^1\| \cdot \|x^2\|, \quad (47)$$

$$\left\| \sum_{i=1}^K x^i \right\|^2 \leq K \sum_{i=1}^K \|x^i\|^2, \quad (48)$$

$$\|x^k - \hat{x}^k\| \leq \sum_{d=k-\epsilon}^{k-1} \|\Delta^d\|. \quad (49)$$

And for any $A \succ 0$, it holds that

$$\lambda_{\min}(A)I \leq A \leq \lambda_{\max}(A)I, \quad (50)$$

$$v^\top A^{-1}v \geq \frac{\|v\|^2}{\lambda_{\max}(A)}, \quad \forall v \in \mathbb{R}^N, \quad (51)$$

$$v^\top Av \geq \lambda_{\min}(A)\|v\|^2, \quad \forall v \in \mathbb{R}^N. \quad (52)$$

where $\lambda_{\max}(A)$ and $\lambda_{\min}(A)$ denote the largest and smallest eigenvalues of A , respectively.

C. Convergence Analysis

After each block update, the global state becomes x^{k+1} , and the objective value decreases according to the L -smoothness property of $f(x)$:

$$\|\nabla f(x) - \nabla f(y)\| \leq L\|x - y\|, \quad \forall x, y \in \mathbb{R}^N, \quad (53)$$

we have:

$$f(x^{k+1}) \leq f(x^k) + \langle \nabla f(x^k), \Delta^k \rangle + \frac{L}{2} \|\Delta^k\|^2. \quad (54)$$

However, since the update is computed using a delayed copy \hat{x}^k , the gradient is evaluated at a stale point, introducing an additional deviation term:

$$f(x^{k+1}) - f(x^k) \leq \langle \nabla f(x^k) - \nabla f(\hat{x}^k), \Delta^k \rangle + \langle \nabla f(\hat{x}^k), \Delta^k \rangle + \frac{L}{2} \|\Delta^k\|^2. \quad (55)$$

The first term of (55) accounts for the delay-induced gradient mismatch, while the second term corresponds to the descent direction in the delayed update. For the first term, we have

$$\langle \nabla f(x^k) - \nabla f(\hat{x}^k), \Delta^k \rangle \leq \|\nabla f(x^k) - \nabla f(\hat{x}^k)\| \cdot \|\Delta^k\| \quad (56a)$$

$$\leq L\|x^k - \hat{x}^k\| \cdot \|\Delta^k\| \quad (56b)$$

$$\leq L \sum_{d=k-\epsilon}^{k-1} \|\Delta^d\| \cdot \|\Delta^k\| \quad (56c)$$

$$\leq \sum_{i=k-\epsilon}^{k-1} \frac{L}{2\epsilon} \|\Delta^i\|^2 + \frac{\epsilon L}{2} \|\Delta^k\|^2, \quad (56d)$$

where (56a) follows from the Cauchy-Schwarz inequality (47), (56b) uses the L -smoothness of f (53), (56c) applies the bounded delay assumption (49), and (56d) employs Young's inequality (46) with parameter $\varepsilon > 0$.

For the second term, using the Levenberg-Marquardt update rule $\Delta^k = -(J^{k\top} J^k + \lambda I)^{-1} J^{k\top} r(\hat{x}^k)$, we have

$$\langle \nabla f(\hat{x}^k), \Delta^k \rangle = -g^{k\top} (J^{k\top} J^k + \lambda I)^{-1} g^k \quad (57a)$$

$$\leq \frac{-\|g^k\|^2}{\lambda_{\max}(J^{k\top} J^k + \lambda I)} \quad (57b)$$

$$\leq \frac{-\|g^k\|^2}{\lambda + \lambda_{\max}(J^{k\top} J^k)} \quad (57c)$$

$$\leq -\frac{1}{\lambda + S^2} \|g^k\|^2 \quad (57d)$$

$$\leq -\frac{1}{\lambda + S^2} \Delta^{k\top} H^{k\top} H^k \Delta^k \quad (57e)$$

$$\leq -\frac{\lambda_{\min}^2(J^{k\top} J^k + \lambda I)}{\lambda + S^2} \|\Delta^k\|^2 \quad (57f)$$

$$\leq -\frac{\lambda^2}{\lambda + S^2} \|\Delta^k\|^2. \quad (57g)$$

where S bounds the largest singular value of J^k , i.e., $\sigma_{\max}(J^k) \leq S$, (57b) and (57f) use the Rayleigh quotient inequalities (51) and (52), respectively.

Substituting the above results, we obtain

$$f(x^{k+1}) - f(x^k) \leq \sum_{i=k-\varepsilon}^{k-1} \frac{L}{2\varepsilon} \|\Delta^i\|^2 + \left[\frac{\varepsilon L}{2} + \frac{L}{2} - \frac{\lambda^2}{\lambda + S^2} \right] \|\Delta^k\|^2. \quad (58)$$

We define a Lyapunov function to facilitate the convergence analysis:

$$\mathcal{L}^k = f(x^k) + \frac{L}{2\varepsilon} \sum_{i=k-\varepsilon}^{k-1} (i - (k - \varepsilon) + 1) \|\Delta^i\|^2, \quad (59)$$

and analyze its descent using (58):

$$\begin{aligned} \mathcal{L}^k - \mathcal{L}^{k+1} &= f(x^k) - f(x^{k+1}) \\ &\quad + \frac{L}{2\varepsilon} \sum_{i=k-\varepsilon}^{k-1} \|\Delta^i\|^2 - \frac{L\varepsilon}{2\varepsilon} \|\Delta^k\|^2 \\ &\geq \left[\frac{\lambda^2}{\lambda + S^2} - \frac{L}{2} - \frac{\varepsilon L}{2} - \frac{L\varepsilon}{2\varepsilon} \right] \|\Delta^k\|^2. \end{aligned} \quad (60)$$

To ensure monotonic descent, we require the coefficient of $\|\Delta^k\|^2$ to be positive, i.e.

$$\alpha \triangleq \frac{\lambda^2}{\lambda + S^2} - \frac{L\varepsilon}{2} - \frac{L}{2} \left(\varepsilon + \frac{1}{\varepsilon} \right), \quad (61)$$

and the coefficient is maximized when $\varepsilon = 1$, leading to the sufficient condition on the LM damping parameter λ :

$$\lambda > \frac{(2L\varepsilon + L) + \sqrt{(2L\varepsilon + L)^2 + 8(2L\varepsilon + L)S^2}}{4}. \quad (62)$$

Summing both sides of (60) from $k = 0$ to $K - 1$ and using

that $\{\mathcal{L}^k\}$ is bounded below by f^* , we have

$$\sum_{k=0}^{K-1} \|\Delta^k\|^2 \leq \frac{\mathcal{L}^0 - \mathcal{L}^K}{\alpha} \leq \frac{\mathcal{L}^0 - f^*}{\alpha} < \infty. \quad (63)$$

Hence $\sum_{k=0}^{\infty} \|\Delta^k\|^2 < \infty$ and in particular $\|\Delta^k\| \rightarrow 0$.

From the Rayleigh quotient bounds (50), we have

$$\|g^k\| = \|H^k \Delta^k\| \leq \lambda_{\max}(H^k) \|\Delta^k\| \leq (\lambda + S^2) \|\Delta^k\|, \quad (64)$$

and

$$\begin{aligned} \|\nabla f(x^k)\| &\leq \|\nabla f(x^k) - \nabla f(\hat{x}^k)\| + \|g^k\| \\ &\leq L \sum_{i=k-\varepsilon}^{k-1} \|\Delta^i\| + (\lambda + S^2) \|\Delta^k\|. \end{aligned} \quad (65)$$

Since $\|\Delta^k\| \rightarrow 0$, the right-hand side tends to zero, and thus

$$\|\nabla f(x^k)\| \rightarrow 0. \quad (66)$$

Consequently, every accumulation point of $\{x^k\}$ is a first-order stationary point of f .

APPENDIX C

CONVERGENCE ANALYSIS FOR INCREMENTAL A-BCD

In state estimation problems, both the number of variables and the number of residuals grow as new measurements arrive. Additionally, in certain parametrizations such as clamped B-spline control points, the values of existing variables may be modified. These dynamics, including new residuals, new variables, and modifications to existing variables, all manifest as changes to the gradient, potentially affecting convergence. To analyze convergence in this setting, we focus on a fixed subset of variables $x = x_{\text{old}} = (x_1, \dots, x_N)$ that were present at the start of the optimization. New variables x_{new} can be added and optimized alongside the old ones. This is without loss of generality: once x_{new} is introduced, it becomes part of the "old" variables in subsequent analysis, and the same convergence guarantee applies. We address the challenge of evolving objectives by treating each iteration as optimizing a frozen target with respect to x_{old} . All sources of change are captured through a single gradient drift bound δ_t , which quantifies the total perturbation to the gradient at each time step.

A. Problem Formulation with Time-Varying Objectives

At iteration k , let $t(k)$ denote the time index when the update begins. The objective function evolves as

$$f_t(x) = \frac{1}{2} \sum_{j=1}^{m_t} \|r_j(x)\|^2, \quad (67)$$

where m_t increases with time t as new measurements arrive. During the k -th update, we compute the step based on the frozen objective $f_{t(k)}$, even though by the time the update completes, the objective may have evolved to $f_{t(k+1)}$ where $t(k+1) \geq t(k)$ (i.e., additional measurements may have arrived during the update).

The update rule remains

$$\Delta^k = -(J_k^\top J_k + \lambda I)^{-1} J_k^\top r(\hat{x}^k), \quad x^{k+1} = x^k + \Delta^k, \quad (68)$$

where J_k and $r(\cdot)$ are evaluated using the objective $f_{t(k)}$ at the delayed state \hat{x}^k .

B. Key Assumptions for Incremental Setting

We require the following additional assumptions beyond those in Appendix B:

Assumption 1 (Gradient Drift Bound). *There exists a sequence $\{\delta_t\}$ such that for all t and all x (or at least on the trajectory $\{x^k + \theta\Delta^k : k \geq 0, \theta \in [0, 1]\}$),*

$$\|\nabla f_{t+1}(x) - \nabla f_t(x)\| \leq \delta_t, \quad (69)$$

with

$$\sum_{t=0}^{\infty} \delta_t < \infty \quad \text{and} \quad \sum_{t=0}^{\infty} \delta_t^2 < \infty. \quad (70)$$

Here, t denotes the discrete index of the evolving objective sequence $\{f_t\}$. Between f_t and f_{t+1} , the objective may change due to any update event. (69) requires that the gradient drift between two objectives f_t and f_{t+1} is bounded by δ_t . At iteration k , the optimizer operates on the frozen objective $f_{t(k)}$. We denote by $\delta_{t(k)}$ the summarized gradient drift between $f_{t(k)}$ and $f_{t(k+1)}$.

C. Convergence Analysis

Following the analysis in Appendix B for the frozen objective $f_{t(k)}$, we obtain

$$\begin{aligned} f_{t(k)}(x^{k+1}) - f_{t(k)}(x^k) &\leq \frac{L}{2\varepsilon} \sum_{i=k-\varepsilon}^{k-1} \|\Delta^i\|^2 \\ &\quad + \left(\frac{\varepsilon\varepsilon L}{2} + \frac{L}{2} - \frac{\lambda^2}{\lambda + S^2} \right) \|\Delta^k\|^2. \end{aligned} \quad (71)$$

However, the actual objective at iteration $k+1$ changes from $f_{t(k)}$ to $f_{t(k+1)}$. we can bound the discrepancy between the successive objectives as follows:

$$\begin{aligned} f_{t(k+1)}(x^{k+1}) - f_{t(k)}(x^{k+1}) &= \int_0^1 \langle \nabla f_{t(k+1)}(x_\theta^{k+1}) - \nabla f_{t(k)}(x_\theta^{k+1}), \Delta^k \rangle d\theta \quad (72a) \\ &\leq \delta_{t(k)} \|\Delta^k\| \leq \frac{\varepsilon}{2} \|\Delta^k\|^2 + \frac{1}{2\varepsilon} \delta_{t(k)}^2, \end{aligned} \quad (72b)$$

where $x_\theta^{k+1} = x^k + \theta\Delta^k$. (72a) follows the mean value theorem and Assumption 1, (72b) uses Cauchy-Schwarz (47) and Young's inequality (46) with parameter $\varepsilon > 0$.

Combining (71) and (72b), we obtain

$$\begin{aligned} f_{t(k+1)}(x^{k+1}) - f_{t(k)}(x^k) &\leq \frac{L}{2\varepsilon} \sum_{i=k-\varepsilon}^{k-1} \|\Delta^i\|^2 \\ &\quad + \left(\frac{\varepsilon\varepsilon L}{2} + \frac{L}{2} + \frac{\varepsilon}{2} - \frac{\lambda^2}{\lambda + S^2} \right) \|\Delta^k\|^2 + \frac{1}{2\varepsilon} \delta_{t(k)}^2. \end{aligned} \quad (73)$$

We define a new Lyapunov function to facilitate the convergence analysis:

$$\mathcal{L}^k = f_{t(k)}(x^k) + \frac{L}{2\varepsilon} \sum_{i=k-\varepsilon}^{k-1} (i - (k - \varepsilon) + 1) \|\Delta^i\|^2, \quad (74)$$

and analyze its descent:

$$\begin{aligned} \mathcal{L}^{k+1} - \mathcal{L}^k &= f_{t(k+1)}(x^{k+1}) - f_{t(k)}(x^k) \\ &\quad - \frac{L}{2\varepsilon} \sum_{i=k-\varepsilon}^{k-1} \|\Delta^i\|^2 + \frac{L\varepsilon}{2\varepsilon} \|\Delta^k\|^2 \quad (75) \\ &\leq -\alpha \|\Delta^k\|^2 + \frac{1}{2\varepsilon} \delta_{t(k)}^2. \end{aligned}$$

where

$$\alpha \triangleq \frac{\lambda^2}{\lambda + S^2} - \frac{\varepsilon}{2} - \frac{\varepsilon L}{2} - \frac{L}{2} - \frac{L\varepsilon}{2\varepsilon}. \quad (76)$$

Choosing $\varepsilon = 1$ and ensuring λ satisfies the sufficient condition as same as in Appendix B (with a minor adjustment for the additional $\varepsilon/2$ term), we guarantee $\alpha > 0$.

Lemma 1 (Robbins-Siegmund [68]). *Let $\{V^k\}$, $\{a^k\}$, and $\{b^k\}$ be sequences of non-negative real numbers satisfying*

$$V^{k+1} \leq V^k - a^k + b^k, \quad \forall k \geq 0. \quad (77)$$

If $\sum_{k=0}^{\infty} b^k < \infty$ and V^k is bounded below, then:

- 1) V^k converges to some finite value $V^* \geq 0$,
- 2) $\sum_{k=0}^{\infty} a^k < \infty$.

We apply Lemma 1 to (75) by identifying

$$V^k = \mathcal{L}^k, \quad a^k = \alpha \|\Delta^k\|^2, \quad b^k = \frac{1}{2\varepsilon} \delta_{t(k)}^2.$$

To verify the conditions of Lemma 1, we note that Assumption 1 ensures

$$\sum_{k=0}^{\infty} b^k = \frac{1}{2\varepsilon} \sum_{k=0}^{\infty} \delta_{t(k)}^2 < \infty,$$

and the Lyapunov function is bounded below by

$$\mathcal{L}^k \geq f_{t(k)}(x^k) \geq f^* \geq 0,$$

where $f^* = \inf_x f(x)$ denotes the infimum of the objective function.

By Lemma 1, we conclude that the sequence $\{\mathcal{L}^k\}$ converges to a finite limit, and

$$\sum_{k=0}^{\infty} \alpha \|\Delta^k\|^2 < \infty.$$

Since $\alpha > 0$, $\sum_{k=0}^{\infty} \|\Delta^k\|^2 < \infty$ and in particular $\|\Delta^k\| \rightarrow 0$.

From $\|\Delta^k\| \rightarrow 0$ and the analysis in Appendix B (analogous to equation (65)), we have

$$\|\nabla f_{t(k)}(x^k)\| \leq L \sum_{i=k-\varepsilon}^{k-1} \|\Delta^i\| + (\lambda + S^2) \|\Delta^k\| \rightarrow 0. \quad (78)$$

Thus, every accumulation point of $\{x^k\}$ is a first-order stationary point of the frozen objectives $f_{t(k)}$.

Convergence to the limiting objective: If the objectives stabilize in the sense that $f_t \rightarrow f_\infty$ as $t \rightarrow \infty$ (e.g., measurements eventually cover a finite region, or $\sum_t \delta_t < \infty$ ensuring uniform gradient convergence), then

$$\|\nabla f_\infty(x^k) - \nabla f_{t(k)}(x^k)\| \leq \sum_{s \geq t(k)} \delta_s \rightarrow 0. \quad (79)$$

Combining this with $\|\nabla f_{t(k)}(x^k)\| \rightarrow 0$, we conclude

$$\|\nabla f_\infty(x^k)\| \rightarrow 0. \quad (80)$$

Therefore, every accumulation point of $\{x^k\}$ is a first-order stationary point of the limiting objective f_∞ .

Remark 6. *In practice, δ_t may arise from new residuals:*

$$\nabla f_{t+1}(x) - \nabla f_t(x) = \sum_{j=m_t+1}^{m_{t+1}} J_j(x)^\top r_j(x). \quad (81)$$

For problems with localized parametrizations (e.g., spline-based trajectories with localized support), each new residual couples only with a bounded subset of variables, ensuring δ_t remains bounded. When the total number of residuals remains finite, the condition $\sum_{t=0}^{\infty} \delta_t^2 < \infty$ holds naturally.

Additionally, δ_t may arise from modifications to existing variables (e.g., clamped B-spline control points), which can also be bounded under B-Splines' localized influence.

Remark 7. *The analysis above based on a L -Lipschitz continuous gradient. In CT-RIO, the residuals are L -smooth as long as arguments remain bounded and away from singularities, which implies that the objective function has a Lipschitz continuous gradient.*

Remark 8. *The analysis above assumes a fair block rule (each block is selected infinitely often) and a bounded delay ϵ . These conditions are satisfied in our IA-BCD implementation of CT-RIO.*

Remark 9. *If some blocks live on differentiable manifolds (e.g., $\text{SO}(3)$), the update should be interpreted in the local tangent space with a smooth retraction $x_i^{k+1} = x_i^k \boxplus \Delta_i^k$. Within a compact trust region, the pulled-back objective remains L -smooth and the Jacobian spectra are uniformly bounded; hence all inequalities and convergence conclusions continue to hold verbatim with norms taken in the corresponding tangent spaces. In practice, modern solvers such as Ceres [64] provide differentiable manifold support that ensures local Euclidean behavior.*